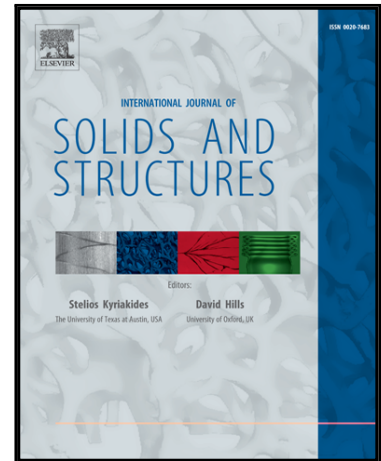# Accepted Manuscript

Evaluation and Calibration of Anisotropic Yield Criteria in Shear Loading: Constraints to Eliminate Numerical Artefacts

A. Abedini , C. Butcher , T. Rahmaan , M.J. Worswick

Please cite this article as: A. Abedini , C. Butcher , T. Rahmaan , M.J. Worswick , Evaluation and Calibration of Anisotropic Yield Criteria in Shear Loading: Constraints to Eliminate Numerical Artefacts, *International Journal of Solids and Structures* (2017), doi: 10.1016/j.ijsolstr.2017.06.029

Highlights

- Phenomenological yield functions may lead to non-physical artefacts in shear region
- These artefacts manifest as non-zero hydrostatic stress or through-thickness strain
- These artefacts can be removed with a calibration constraint proposed in the paper

Evaluation and Calibration of Anisotropic Yield Criteria in Shear Loading: Constraints to Eliminate Numerical Artefacts

A. Abedini[*], C. Butcher, T. Rahmaan, M.J. Worswick

Department of Mechanical and Mechatronics Engineering, University of Waterloo, Waterloo, ON, CANADA

[*]Corresponding author. Email: aabedini@uwaterloo.ca

Abstract: Many anisotropic phenomenological yield functions have been proposed in the literature in which their predictive capabilities strongly depend on the experimental calibration data as well as the calibration procedure to identify the anisotropy parameters. In this paper, emphasis is placed upon the experimental and numerical calibration procedure of anisotropic yield functions in the region of shear loading (zero hydrostatic stress with equal and opposite in-plane principal strains and stresses). Conventional anisotropic calibration procedures are shown to introduce non-physical artefacts into constitutive models which manifest as a non-zero hydrostatic stress or through-thickness strains generated under in-plane shear stress that violate the definition of the shear loading condition. To overcome this issue, a new physically necessary constraint is applied on the plastic potential to enforce equal and opposite principal strains in the shear state and correct the shear region of anisotropic yield functions. Using this necessary constraint, the widely used Yld2000-2d anisotropic yield function was calibrated using an associated flow rule for aluminum alloy sheet using published data for AA2090-T3 to demonstrate how enforcing this constraint can be readily implemented to correct the shear region of the anisotropic yield surface. Furthermore, to investigate the influence of the shear constraint, an AA7075-T6 alloy was experimentally characterized in uniaxial tension, equal-biaxial tension and shear. It was revealed that with the additional shear constraints, non-physical artefacts of plane-stress anisotropic yield functions such as Yld2000-2d can be removed during the calibration procedure. However, due to the additional shear constraints, available anisotropic models may become over-constrained and alternate yield functions with more flexibility or non-associated flow rules may be required.

Keywords: Shear deformation; anisotropic material; constitutive characterization; calibration constraint

1. Introduction

Many commercial sheet metal alloys used in forming operations exhibit anisotropic plastic behaviour. Plastic anisotropy can be a result of different features but the non-random distribution of crystal orientations due to manufacturing processes (such as rolling and extrusion) is the major reason for orientation-dependent plastic behaviour. Therefore, isotropy is no longer an appropriate assumption to represent the mechanical behaviour of these materials. Furthermore, sheet metal forming and crashworthiness simulations rely on an accurate description of yielding behaviour of materials, thus using an appropriate anisotropic constitutive model is an essential step for modelling the plastic deformation of sheet metals (Abedrabbo *et al.*, 2007; Banabic *et al.*, 2010).

Many phenomenological yield functions have been proposed to predict the isotropic and anisotropic plastic behaviour of sheet metals. The quadratic von Mises yield function is one of the oldest isotropic models and still popular in industry and academia. Hershey (1954), and Hosford (1972) proposed non-quadratic isotropic yield functions to obtain better accuracy than the von Mises yield criterion for materials with bcc and fcc crystal microstructures. One of the first anisotropic yield functions was proposed by Hill (1948), also known as the Hill48 model. This model resulted in acceptable predictions for traditional steels; however, with the advent of more advanced steel alloys and the adoption of non-ferrous metals, it was experimentally observed that the Hill48 model was not able to describe the yield surfaces of these metals appropriately (Aretz and Barlat, 2013). Later, Hill proposed various anisotropic yield functions (*e.g.* Hill, 1979; Hill, 1993) to correct the shortcomings and anomalous responses of the Hill48 model but, the popularity of the Hill48 model persists due to its simplicity and availability in most commercial FE software packages.

Major contributions towards the development of anisotropic phenomenological yield functions are manifest in the Barlat family of yield criteria (Barlat and Lian, 1989; Barlat *et al.*, 1991; Barlat *et al.*, 1997; Barlat *et al.*, 2003; Barlat *et al.*, 2005). In 1989, Barlat and Lian proposed the Yld89 yield function (Barlat and Lian, 1989) by modifying the isotropic Hosford (1972) model with a linear transformation of the stress tensor. This methodology became the cornerstone for subsequent Barlat anisotropic functions as isotropic yield functions are used as generators for the development of anisotropic models. The use of linear transformations enables the isotropic

3

models to account for anisotropy while preserving convexity and ensuring incompressibility of plastic flow (independent of hydrostatic stress). Following this procedure, Yld91 (Barlat *et al.*, 1991), Yld94, and Yld96 (Barlat *et al.*, 1997) were proposed to improve the accuracy of the yield functions. In 2003, Yld2000-2d was proposed (Barlat *et al.*, 2003) which is a commonly used yield function for 2-D plane-stress anisotropic modelling of sheet metals. To account for 3-D stress states, Barlat *et al.* (2005) generalized the Yld2000-2d to consider all six components of the stress tensor which resulted in the Yld2004-18p yield criterion. Although the Yld2004-18p model is more expensive computationally, it has been successfully used in simulation of plastic deformations for different grades of aluminum alloys (Yoon *et al.*, 2006; Fourmeau *et al.*, 2011; Tardif and Kyriakides, 2012).

The transformation approach is carried out using single or multiple linear transformations of the stress tensor (or stress deviator). The components of the transformation tensors are calibration coefficients whose values are obtained by minimizing the difference between the predictions of yield functions with the experimental tests in different loading conditions and test orientations. In most of the papers cited above, uniaxial and equal-biaxial yield stresses and r-values were used to calibrate the anisotropic yield functions. Implicit in the Barlat-type and most anisotropic constitutive models is the assumption of an associated flow rule although the models can be extended to non-associated flow (Safaei *et al.*, 2013) so that both the stress ratios and r-values are calibrated together (associated flow rule) or separately in non-associated flow with the stress ratios used to calibrate the yield function and the r-values the flow rule. For a plane-stress anisotropic model, typical calibration experiments involve tensile tests in three orientations relative to the rolling direction of the sheet and an equal-biaxial test with each test providing both a stress ratio and r-value for a total of eight measurements that can be used to calibrate a yield function such as the Yld2000-2d with eight parameters (Barlat *et al.*, 2003). For a non-associated version of the Yld2000-2d, additional tensile tests are performed in seven orientations along with the equal-biaxial test to obtain eight stress ratios and eight r-values to calibrate the yield criterion and flow rule independently. Similar approaches are required for 3-D anisotropic models with seven tensile tests and an equal-biaxial test, then usually assumptions are made for the stress ratios and r-values within the thickness direction since these experiments cannot be performed for sheet materials. These calibrated anisotropic models are then commonly employed in sheet metal forming and crashworthiness simulations.

4

Unfortunately, this type of calibration does not guarantee that the predictions of yield functions are accurate in the shear state. Although shear tests for plastic constitutive characterization of sheet metals are gaining more attention in the literature (*e.g.* Zang *et al.*, 2011; Steglich *et al.*, 2016; Abedini *et al.*, 2017a,b), there is a lack of comprehensive studies of calibration of yield functions in the shear region. The purpose of the present study is to demonstrate the constraints that should be imposed for calibration of anisotropic yield functions in the shear region and to critically evaluate the consequences of the lack of these constraints in terms of hydrostatic stress and strain path predictions. These constraints follow directly from the mechanics of shear deformation and are imposed on the plastic potential function (or yield function in associated flow) to enforce equal and opposite principal strains in the shear regions with zero hydrostatic stress. The results of this study shed light into the need for accurate calibration of anisotropic yield functions in the shear stress state region which has received limited attention in the literature.

2. Continuum-based Plasticity

Phenomenological yield functions and flow rules establish the framework of continuum-based plasticity. A generic yield function, Φ, can be introduced as:

$$\Phi(\boldsymbol{s}, \alpha_i, a, \varepsilon_{eq}^p) = \sigma_{eq} \tag{1}$$

where σ_{eq} is the equivalent stress which is a function of the stress deviator, **s**, anisotropy parameters, α_i, the yield exponent, a, and the equivalent plastic strain ε_{eq}^p. Note that in the present paper, boldface italicized letters refer to 2nd order tensors and boldface capital letters refer to 4th order tensor quantities. Similarly, a flow potential function, $\Psi(\boldsymbol{s}, \beta_i, b, \varepsilon_{eq}^p)$, is defined with anisotropy parameters, β_i, and the yield exponent, b, that are independent from yield function. The plastic strain increments are normal to the flow potential for a given stress state and expressed as:

$$d\boldsymbol{\varepsilon}^p = d\lambda \, \frac{\partial \Psi}{\partial \boldsymbol{\sigma}} \tag{2}$$

5

where $d\lambda$ is the scalar plastic multiplier and σ is the stress tensor. Using the principal of plastic work equivalence and assuming that the plastic potential is a first-order homogeneous function, the following relation can be used to calculate the work-conjugate equivalent plastic strain (Cvitanic *et al.,* 2008):

$$d\varepsilon_{\mathrm{eq}}^{\mathrm{p}} = d\lambda \; \frac{\Psi}{\Phi} \tag{3}$$

For an associated flow rule, the yield and plastic potential functions are identical ($\Phi = \Psi$), and Eq. (3) reduces to:

$$d\varepsilon_{\mathrm{eq}}^{\mathrm{p}} = d\lambda \tag{4}$$

The well-known anisotropic yield function of Yld2000-2d of Barlat *et al.* (2003) is employed in the present study which is briefly given in what follows, while detailed description can be found in Barlat *et al.* (2003). It is assumed that the material has three mutually orthotropic anisotropic axes denoted as x_1, x_2, and x_3 which, are taken to correspond to the sheet rolling direction (RD), transverse direction (TD), and normal (thickness) direction (ND), respectively. The equivalent stress associated with the Yld2000-2d yield function is written as:

$$\sigma_{\mathrm{eq}}^{\mathrm{Yld2000}} = \left(\frac{\phi' + \phi''}{2} \right)^{1/a} \tag{5}$$

where ϕ' and ϕ'' are written as:

$$\phi' = \left| X_1' - X_2' \right|^a \;, \quad \phi'' = \left| 2X_2'' + X_1'' \right|^a + \left| 2X_1'' + X_2'' \right|^a \tag{6,7}$$

in which X_i' and X_i'' are the principal values of the linearly transformed stress tensors, $\boldsymbol{X'}$ and $\boldsymbol{X''}$, that are written as:

$$\boldsymbol{X'} = \mathbf{L'} : \boldsymbol{\sigma} \;, \quad \boldsymbol{X''} = \mathbf{L''} : \boldsymbol{\sigma} \tag{8,9}$$

where ":" denotes the doubled contracted product between two tensors. The fourth-order linear stress transformation tensors are $\mathbf{L'}$ and $\mathbf{L''}$ and can be reduced for plane-stress loading to:

$$\boldsymbol{L'} = \begin{bmatrix} L'_{11} & L'_{12} & 0 \\ L'_{21} & L'_{22} & 0 \\ 0 & 0 & L'_{66} \end{bmatrix} \quad , \quad \boldsymbol{L''} = \begin{bmatrix} L''_{11} & L''_{12} & 0 \\ L''_{21} & L''_{22} & 0 \\ 0 & 0 & L''_{66} \end{bmatrix} \tag{10,11}$$

and are defined as:

$$\begin{bmatrix} L'_{11} \\ L'_{12} \\ L'_{21} \\ L'_{22} \\ L'_{66} \end{bmatrix} = \begin{bmatrix} 2/3 & 0 & 0 \\ -1/3 & 0 & 0 \\ 0 & -1/3 & 0 \\ 0 & 2/3 & 0 \\ 0 & 0 & 1 \end{bmatrix} \begin{bmatrix} \alpha_1 \\ \alpha_2 \\ \alpha_7 \end{bmatrix} \quad , \quad \begin{bmatrix} L''_{11} \\ L''_{12} \\ L''_{21} \\ L''_{22} \\ L''_{66} \end{bmatrix} = \frac{1}{9} \begin{bmatrix} -2 & 2 & 8 & -2 & 0 \\ 1 & -4 & -4 & 4 & 0 \\ 4 & -4 & -4 & 1 & 0 \\ -2 & 8 & 2 & -2 & 0 \\ 0 & 0 & 0 & 0 & 9 \end{bmatrix} \begin{bmatrix} \alpha_3 \\ \alpha_4 \\ \alpha_5 \\ \alpha_6 \\ \alpha_8 \end{bmatrix} \tag{12,13}$$

where α_i are the anisotropy coefficients that should be calibrated with experimental data. In the case of isotropy, all of the α_i coefficients are set to unity. Note that the derivatives of the anisotropic yield function of Yld2000-2d and closed-form equations as functions of anisotropy coefficients to calculate the equivalent stress under different stress states are given in Barlat *et al.* (2003) and Yoon *et al.* (2004), and are not provided here for brevity. The value of the exponent of the yield function "*a*" in Eq. (5) is commonly set to 6 for bcc and 8 for fcc materials as suggested by Barlat *et al.* (2003). It can be seen from Eqs. (12,13) that the Yld2000-2d yield function contains eight anisotropy coefficients, α_{1-8}, that can be calibrated with experimental data as explained in the next section.

3. Conventional Calibration Method for Anisotropic Yield Functions

The values of the anisotropy coefficients in the transformation tensors (Eqs. 12,13) are generally determined from experimental data using a series of tests in proportional stress states in uniaxial tension tests in multiple sheet orientations and an equal-biaxial tension test. This method of calibration has been extensively used in the literature to calibrate various anisotropic yield functions (*e.g.* Barlat *et al.*, 2003; Yoon *et al.*, 2004; Barlat *et al.*, 2005; Yoon *et al.*, 2006; Hassannejadasl *et al.*, 2014) and will be referred to as the "conventional calibration method".

Uniaxial tension tests are classical experiments performed for constitutive characterizations and are usually reported as yield stresses in three orientations of 0° (rolling direction or RD), 45°

(diagonal direction or DD), and 90° (transverse direction or TD). The stress measurements are usually expressed as a ratio relative to a reference direction (usually the rolling direction). Other important values obtained from uniaxial tests are the r-values with the definition of:

$$r = \frac{d\varepsilon_2^{\mathrm{p}}}{d\varepsilon_3^{\mathrm{p}}} \tag{14}$$

where $d\varepsilon_2^{\mathrm{p}}$ and $d\varepsilon_3^{\mathrm{p}}$ are the respective plastic increments in the width and thickness directions of the tensile specimen. The r-values are also reported in the three directions of the RD (r_0), DD (r_{45}), and TD (r_{90}). In addition to the uniaxial tensile tests, the equal-biaxial tensile yield stress, σ_b, and r-value, r_b, can be calculated using cruciform (*e.g.* Kuwabara *et al.*, 1998), bulge (e.g. Kaya *et al.*, 2008), or through-thickness compression tests (*e.g.* Steglich *et al.*, 2014) to calibrate the equal-biaxial tensile region of anisotropic yield functions. The equal-biaxial r-value is defined as:

$$r_b = \frac{d\varepsilon_{\mathrm{TD}}^{\mathrm{p}}}{d\varepsilon_{\mathrm{RD}}^{\mathrm{p}}} \tag{15}$$

For many of engineering alloys, both stress ratios and r-values can be assumed to remain constant with plastic deformation, therefore, the r-values in Eqs. (14) and (15) are commonly written in terms of the total strain components as:

$$r = \frac{\varepsilon_2^{\mathrm{p}}}{\varepsilon_3^{\mathrm{p}}} \quad , \quad r_b = \frac{\varepsilon_{\mathrm{TD}}^{\mathrm{p}}}{\varepsilon_{\mathrm{RD}}^{\mathrm{p}}} \tag{16,17}$$

If the experimental stress ratios and r-values are not constant with deformation, as observed in magnesium alloys (Ghaffari Tari *et al.,* 2014; Abedini *et al.,* 2017b), then the anisotropy coefficients can be calibrated as a function of plastic deformation (*e.g.* Cai *et al.*, 2016). Note that for hcp materials such as magnesium alloys that have tension-compression asymmetry, in addition to the tests described above, compression tests would be included in the conventional calibration (Abedini *et al.*, 2017b).

It is worth mentioning that an alternative option to the conventional calibration method is to use the virtual fields method (VFM) such as in Fu *et al.* (2016) and Rossi *et al.* (2016), or to use

complex test geometries with heterogeneous strains fields along with inverse tools to calibrate the coefficients of anisotropic models (*e.g.* Souto *et al.*, 2015; 2016a,b). Although these methods will not be considered in the present study, the shear constraints developed in subsequent sections will also be applicable to these alternate calibration strategies.

In order to determine the values of the anisotropy coefficients, an optimization approach can be used to minimize the errors between the experimental data and the values predicted by the anisotropic yield functions. The procedures for this optimization are well-established and documented in the literature (Barlat *et al.*, 2003; 2005) and often involve a least-squares minimization performed with different optimization methodologies and weighting parameters are introduced for the different experimental data points to obtain a preferred calibration. In the present study, the genetic algorithm (GA) (Sivanandam and Deepa, 2008) was selected to perform the minimization which is a global optimization subroutine available in Matlab®. The "*Error*" function is:

$$Error = w_\sigma \sum_{i=1}^{m} \left(\left(\frac{\sigma_{\mathrm{model}}}{\sigma_{\mathrm{exp}}} \right)_i - 1 \right)^2 + w_\mathrm{r} \sum_{i=1}^{m} \left(\left(\frac{r_{\mathrm{model}}}{r_{\mathrm{exp}}} \right)_i - 1 \right)^2 \qquad (18)$$

in which the superscripts "exp" and "model" in Eq. (18) indicate either measured values or predicted quantities from anisotropic yield function. Moreover, w_σ and w_r are weighting values for stresses and r-values, respectively, and "*m*" is the number of available experimental data points. Note that since yield criteria are adopted for plastic behaviour of materials, variables such as stress and strain tensors are non-zero at the onset of yielding and the denominators in Eq. (18) are non-zero.

For the GA, the population size and the fraction of parent-to-children populations were set to 100 and 0.35, respectively. Furthermore, the Matlab® defaults for the crossover fraction and mutation function were employed. The maximum number of generations in each optimization was set to 300, and each optimization loop ends if the value of *Error* is below a tolerance (set to 0.001) or when the maximum number of generations was reached. It is shown in the literature that the GA is a robust optimization method with enhanced performance compared to least square regression analysis (Jenab *et al.*, 2016). However, it is important to note that although the GA optimization algorithm was used in the present study, alternative optimization approaches (*e.g.* Newton-

Raphson method in Barlat *et al*., 2003) could also be used to perform the minimization of Eq. (18) to similar or even higher accuracy. The focus of the present work is not to identify the best optimization algorithm but on the identification and enforcement of constraints upon the calibration to ensure physically valid solutions are obtained for shear loading (Section 4). These constraints are independent of the calibration method and can therefore be implemented into the calibration methodology and optimization strategy of choice.

In the present work, the conventional method of calibration was employed with the adopted weighting parameters of $w_\sigma = 1.0$ and $w_r = 0.1$. These weighting values can be selected based on a variety of criteria. For example, depending on the level of uncertainty in the characterization experiments, some of the data may be given more or less weight. Moreover, in finite element simulations using anisotropic yield functions, it is usually preferred to obtain stress values with high accuracy to better capture the load response such as the punch force required in a forming operation. Furthermore, it has been observed that calibration of the yield stresses is often more challenging compared to the calibration of the r-values which also motivates w_σ having a higher value than w_r. The results of the calibration with the conventional method are presented in Section 6.1. However, it will be shown that the conventional calibration method may lead to introduction of some non-physical artefacts into the constitutive response of materials in shear loading condition, highlighting the necessity to develop modified approaches for calibration of anisotropic yield functions.

4. Mechanics of Shear Deformation

In addition to the tests described above, the shear stress state will also be used in the present study to evaluate and calibrate anisotropic yield functions. In continuum mechanics, the shear state is often described using "simple shear" deformation rather than "pure shear" as simple shear state is a closer estimate to what is experimentally performed for constitutive characterization of materials in shear. In pure shear, the principal stress and strain directions are aligned (coaxial) and there is no induced rotation or spin. In simple shear, the principal stress and strain directions are initially aligned but rotate at different rates with deformation so they do not remain coaxial at finite strains. However, at low strain levels such as below 20%, pure and

10

simple shear can be considered equivalent (van den Boogaard, 2002). Perhaps most important in the context of this study is that both simple and pure shear deformations satisfy the conditions for both plane-stress and plane-strain loading and requires that there be no hydrostatic stress. The individual normal stress components may be non-zero, but they must sum to zero. The present section describes the fundamentals of mechanics of deformation in simple shear condition.

4.1. Stress and Strain Tensors

The deformation gradient, F, for simple shear loading applied in the x_1-x_2 plane (Figure 1) can be written as:

$$F = \begin{bmatrix} 1 & \gamma & 0 \\ 0 & 1 & 0 \\ 0 & 0 & 1 \end{bmatrix} \quad \gamma = \tan(\theta) \tag{19}$$

where θ is the shear angle. The deformation gradient can be decomposed via the polar decomposition:

$$F = RU \tag{20}$$

The rotation tensor, R, and the right stretch tensor, U, have been derived by Zhou *et al.* (2003) and Onaka (2010) for simple shear loading as:

$$R = \begin{bmatrix} \dfrac{2}{\sqrt{4+\gamma^2}} & \dfrac{\gamma}{\sqrt{4+\gamma^2}} & 0 \\ \dfrac{-\gamma}{\sqrt{4+\gamma^2}} & \dfrac{2}{\sqrt{4+\gamma^2}} & 0 \\ 0 & 0 & 1 \end{bmatrix} \quad , \quad U = \begin{bmatrix} \dfrac{2}{\sqrt{4+\gamma^2}} & \dfrac{\gamma}{\sqrt{4+\gamma^2}} & 0 \\ \dfrac{\gamma}{\sqrt{4+\gamma^2}} & \dfrac{2+\gamma^2}{\sqrt{4+\gamma^2}} & 0 \\ 0 & 0 & 1 \end{bmatrix} \tag{21,22}$$

Furthermore, the velocity gradient, L, and the rate of deformation tensor, D, that is the objective rate of the logarithmic strain are:

$$L = \dot{F}F^{-1} = \begin{bmatrix} 0 & d\gamma & 0 \\ 0 & 0 & 0 \\ 0 & 0 & 0 \end{bmatrix} \quad , \quad D = \frac{1}{2}(L+L^T) = \begin{bmatrix} 0 & d\gamma/2 & 0 \\ d\gamma/2 & 0 & 0 \\ 0 & 0 & 0 \end{bmatrix} \tag{23,24}$$

11

The logarithmic strain tensor can be written as (Onaka, 2010):

$$\boldsymbol{\varepsilon} = \ln \boldsymbol{U} = \frac{\sinh^{-1}(\gamma/2)}{\sqrt{4+\gamma^2}} \begin{bmatrix} \gamma & 2 & 0 \\ 2 & -\gamma & 0 \\ 0 & 0 & 0 \end{bmatrix} \qquad (25)$$

The eigenvalues of the logarithmic strain rate (Eq. 24) and strain tensor (Eq. 25) correspond to the principal strain increments and principal strains:

$$eig(\boldsymbol{D}) = \begin{bmatrix} d\varepsilon_1 \\ d\varepsilon_2 \\ d\varepsilon_3 \end{bmatrix} = \begin{bmatrix} d\gamma/2 \\ -d\gamma/2 \\ 0 \end{bmatrix} \ , \ eig(\boldsymbol{\varepsilon}) = \begin{bmatrix} \varepsilon_1 \\ \varepsilon_2 \\ \varepsilon_3 \end{bmatrix} = \begin{bmatrix} \sinh^{-1}(\gamma/2) \\ -\sinh^{-1}(\gamma/2) \\ 0 \end{bmatrix} \qquad (26,27)$$

In which ε_{1-3} are the principal strains. Note that Eqs. (26,27) follow directly from the imposed deformation gradient for simple shear in Eq. (19) and are valid for both isotropic and anisotropic materials. Furthermore, it can be seen from Eqs. (26,27) that the principal strains are equal and opposite in simple shear, *i.e.*:

$$\frac{d\varepsilon_2}{d\varepsilon_1} = \frac{\varepsilon_2}{\varepsilon_1} = -1 \qquad (28)$$

To provide experimental evidence that the principal strains are equal and opposite in simple shear loading as in Eq. (28), the evolution of principal strains in the gauge area of a shear experiment on AA7075-T6 alloy is shown in Figure 2 (a detailed description of the shear experiments are given in Section 5). It can be seen that the strain path of the shear test lies almost perfectly on the $\varepsilon_1 = -\varepsilon_2$ line, as expected for a shear condition with plastic volume conservation (without through-thickness strains). Similar strain paths were achieved in Abedini *et al*. (2015), Abedini *et al*. (2017a), and Rahmaan *et al*. (2017) for several grades of steel and aluminum alloy sheet with different degrees of anisotropy using two different types of shear specimens.
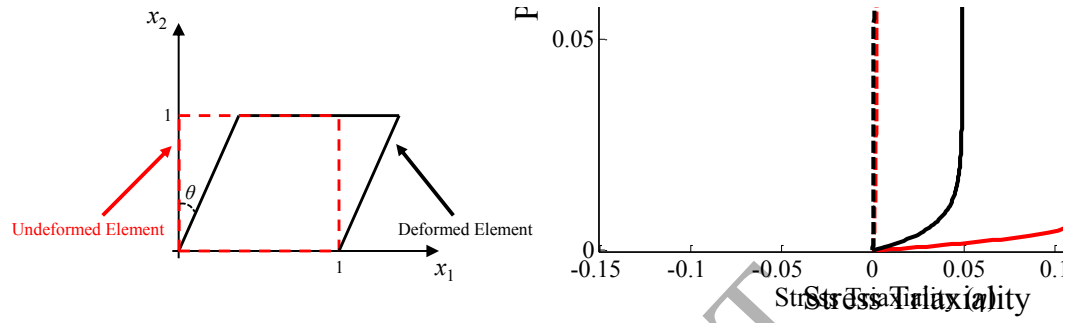
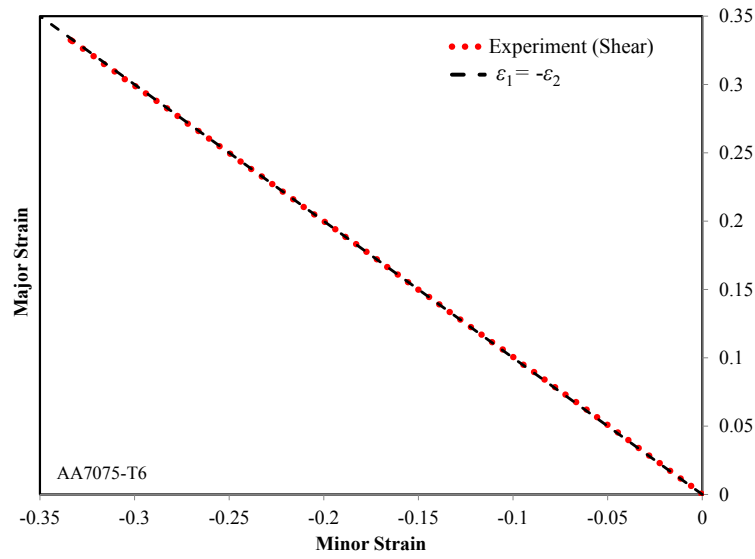Figure 1 – An element in simple shear.

Figure 2 – Strain path in the gauge area for shear tests of AA7075-T6. Similar strain paths were achieved in Abedini *et al.* (2015, 2017a) and Rahmaan *et al.* (2017) for different materials with different degrees of anisotropy using the shear specimen of Peirs *et al.* (2012) as well as a butterfly-type shear specimen developed by Dunand and Mohr (2011).

Furthermore, the stress tensor $\boldsymbol{\sigma}$ in simple shear loading may contain both shear and normal components but the normal components must be deviatoric as there can be no hydrostatic stress:

$$\boldsymbol{\sigma} = \begin{bmatrix} \sigma_{11} & \sigma_{12} & 0 \\ \sigma_{12} & \sigma_{22} & 0 \\ 0 & 0 & 0 \end{bmatrix} \quad , \quad \sigma_{11} = -\sigma_{22} \tag{29}$$

13

For low levels of deformation, the normal stresses are vanishingly small and the familiar infinitesimal result for the stress tensor in shear loading is obtained:

$$\boldsymbol{\sigma} = \begin{bmatrix} 0 & \sigma_{12} & 0 \\ \sigma_{12} & 0 & 0 \\ 0 & 0 & 0 \end{bmatrix} \tag{30}$$

The formation of the normal stress components is due to the induced rotation of the material and is dependent upon the type of objective stress rate used in the stress integration. Recently, Rahmaan *et al*. (2017) adopted a non-quadratic isotropic yield function with a power law hardening law and integrated the stress state using the logarithmic stress rate to a strain level of 100%. It was observed that that the normal stresses remained negligible relative to the magnitude of the shear stress in plastic deformation so that Eq. (30) can be assumed to be reasonable for low to moderate strain levels used for anisotropic yield function calibration.

The principal values, $\sigma_{1\text{-}3}$, of the stress tensor in Eq. (30) are written as:

$$eig(\boldsymbol{\sigma}) = \begin{vmatrix} \sigma_1 \\ \sigma_2 \\ \sigma_3 \end{vmatrix} = \begin{vmatrix} \sigma_{12} \\ -\sigma_{12} \\ 0 \end{vmatrix} \quad , \quad \frac{\sigma_2}{\sigma_1} = -1 \tag{31,32}$$

Consequently, it can be seen that, in a similar manner to the principal strains, principal stresses are equal and opposite in simple shear condition. Moreover, it can be seen that the hydrostatic stress defined by Eq. (33) remains zero under simple shear deformation:

$$\sigma_{\text{hyd}} = \frac{\sigma_{11} + \sigma_{22} + \sigma_{33}}{3} = \frac{\sigma_1 + \sigma_2 + \sigma_3}{3} = 0 \tag{33}$$

4.2. Principal Directions

It was shown in Section 4.1 that the principal strains and principal stresses are equal and opposite in simple shear. However, the principal directions of the stress and strain tensors are not necessarily coaxial. The eigenvectors of the strain tensor of Eq. (25) correspond to the principal directions and can be determined for a given level of shear deformation by (Jonas *et al.,* 2012):

14

$$\vartheta = \frac{1}{2}\tan^{-1}(\frac{2}{d\gamma}) \tag{34}$$

It can be calculated by Eq. (34) that the principal directions of the strain tensor are oriented $\pm 45°$ with respect to the loading direction (*i.e.* x_1, see Figure 1) for zero strain while they continuously deviate from these directions for larger strains. Moreover, the principal directions of the stress tensor in Eqs. (29,30) are orientated $\pm 45°$ with respect to the loading direction for small deformations. Analogously to the strain tensor, the principal directions of the stress tensor rotate with deformation while the rate of the rotation is related to the adopted objective stress rate. For the purposes of this paper, we assume that the strains remain small. It was shown by van den Boogaard (2002) that for small plastic strains of 20% or less, the principal directions of the stress and strain tensors are closely aligned in simple shear. The deviation between the principal strain and stress directions is certainly a complicating issue (see for example Jonas *et al.,* 2012) but it will be shown in Section 6 that this is not the source of the spurious hydrostatic stress predictions by anisotropic yield criteria. However, for low strain levels commonly used for yield function calibration, the principal frames are approximately aligned. In the limit, if the yield criterion is calibrated at a strain corresponding to the onset of yielding at a strain level of 0.2% or other small plastic strains, the misalignment of the principal stress and strain directions can be neglected.

Therefore, in the context of this study that deals with the calibration of anisotropic yield criteria, it will be assumed that the principal stresses and strains are equal and opposite in simple shear. Furthermore, the principal directions of the stress and strain tensors are orientated $\pm 45°$ with respect to the loading direction for the onset of deformation while their principal directions remain closely aligned for small strains.

Note that the Swift phenomenon (occurrence of axial plastic deformation during monotonic free-end torsion of solid rods or tubes which was first observed by Swift, 1947) violates the condition of Eq. (28). Recently, Cazacu *et al.* (2013) related the Swift effect to tension-compression asymmetry of materials and Swift effects occur mostly due to twinning mechanisms in materials with hcp crystal structure (Guo *et al.*, 2013) and will not be considered in the present work that will focus upon sheet materials with cubic crystal structures such as steel and aluminum alloys.

4.3. Shear Constraint

In the light of the mechanics of shear deformation described in Sections 4.1 and 4.2, a new variable, ξ, is defined as the ratio of principal strains operative during shear tests from the deformation gradient (Eq. 19) and the definition of the logarithmic strain rate (Eq. 26). The value of the incremental strain ratio, ξ, as shown in Eq. (28), should be equal to -1 and becomes a constraint upon the plastic calibration that must be enforced upon the anisotropic material model. For example, if we assume that the material is rigid-plastic, for shear in the x_1-x_2 plane:

$$\xi(\sigma_1 = -\sigma_2) = \frac{d\varepsilon_2}{d\varepsilon_1} = -1 \;\Rightarrow\; \frac{d\varepsilon_2^{\mathrm{p}}}{d\varepsilon_1^{\mathrm{p}}} = -1 \;\Rightarrow\; \frac{\dfrac{\partial \Psi}{\partial \sigma_2}}{\dfrac{\partial \Psi}{\partial \sigma_1}} = -1 \tag{35}$$

Furthermore, for an associated flow rule, Eq. (35) reduces to:

$$\xi = -1 \;\overset{\text{Associated Flow Rule}}{\Longrightarrow}\; \frac{\dfrac{\partial \Phi}{\partial \sigma_2}}{\dfrac{\partial \Phi}{\partial \sigma_1}} = -1 \tag{36}$$

To visualize the role of the constraint, a yield surface can be considered in σ_{11}-σ_{22}-σ_{12} space on which the locations of the shear stress state are represented by the intersection of the $\sigma_{11} = -\sigma_{22}$ plane with the yield surface, as shown by the red curve in Figure 3a. All shear loading conditions within the x_1-x_2 plane are located along this curve and their corresponding stress tensor has the form of:

$$\boldsymbol{\sigma} = \begin{bmatrix} \sigma_{11} & \sigma_{12} & 0 \\ \sigma_{12} & -\sigma_{11} & 0 \\ 0 & 0 & 0 \end{bmatrix} \;,\quad \sigma_1 = -\sigma_2 = \sqrt{\sigma_{11}^2 + \sigma_{12}^2} \;,\quad \sigma_3 = 0 \tag{37}$$

Note that all components of the stress tensor vary along the red curve in Figure 3a while the hydrostatic stress always remains zero due to the fact that the principal stresses are equal and opposite ($\sigma_1 = -\sigma_2$), and $\sigma_3 = 0$. The relation in Eq. (35) shows that the value of the principal strain ratio, ξ, is equal to -1 all along this curve and is independent of the employed yield

criterion and flow rule since it comes directly from the deformation gradient. For an anisotropic material, the shear yield stress ratio obtained along the red curve may vary as the loading direction varies but the hydrostatic stress must remain zero and the incremental strain ratio must be -1.

It is interesting to observe that for an isotropic yield criterion such as the non-quadratic Hosford model (Hosford, 1972), the constraint condition of Eq. (35) is automatically satisfied. The plane-stress formulation of the Hosford model is:

$$\sigma_{eq}^{Hosford} = \left\{ \frac{|\sigma_1 - \sigma_2|^a + |\sigma_1|^a + |\sigma_2|^a}{2} \right\}^{1/a} \tag{38}$$

Assuming the associated flow rule and an even number for the exponent (as mentioned earlier, $a=6$ and $a=8$ are commonly used for bcc and fcc materials, respectively), strain ratios in the Hosford model can be calculated using Eq. (2):

$$\frac{d\varepsilon_2}{d\varepsilon_1} = \frac{\left(\frac{\sigma_2}{\sigma_1}\right)^{a-1} - (1 - \frac{\sigma_2}{\sigma_1})^{a-1}}{1 + (1 - \frac{\sigma_2}{\sigma_1})^{a-1}} \Rightarrow \frac{d\varepsilon_2}{d\varepsilon_1}(\sigma_1 = -\sigma_2) = \xi = -1 \tag{39}$$

Eq. (39) is also valid for the von Mises yield function that is a special case of the Hosford criterion with $a=2$. Note that considering a 3-D formulation for yield functions with all the six components of the stress tensor, Eq. (35) should also be satisfied in the spaces of σ_{11}-σ_{33}-σ_{13} and σ_{22}-σ_{33}-σ_{23} as well and their corresponding experimental shear data can be used to calibrate yield functions. However, for rolled sheet metals, shear data in the out-of-plane directions are not usually available, thus shear tests are commonly limited to the x_1-x_2 or RD-TD plane. Within the RD-TD plane, the stress tensor of shear tests is given by Eq. (37), and the orientation of an element subjected to maximum shear stress can be determined by:

$$\bar{\theta}_{Max.Shear} = \frac{1}{2}\tan^{-1}(\frac{\sigma_{11}}{\sigma_{12}}) \tag{40}$$

Using Eq. (40), Point ① in Figure 3a (with $\sigma_{12}=0$) corresponds to the shear state with the applied shear load in the 45° orientation with respect to the rolling direction and the principal directions are initially aligned in the rolling and transverse directions of the sheet.

17

Point ② in Figure 3a (with $\sigma_{11}=\sigma_{22}=0$) belongs to a shear test with the applied load in the RD or equivalently TD directions for orthotropic sheet metals (Lopes *et al.,* 2003; Abedini *et al.,* 2017b). The principal stresses of this point are along the 45° and 135° directions.

Finally, Point ③ in Figure 3a has a stress state similar to Point ①; however, the signs of the principal stresses are interchanged, indicating that the shear test is in the 135° orientation with respect to the RD. Note that as shown in Figure 3b, Points ① and ③ are located in the 4th and 2nd quadrants of the yield locus, respectively.

It is worth re-iterating that due to anisotropy, the shear yield stresses along the red curve in Figure 3a may vary while the hydrostatic stress must be enforced to be zero as the stress state remains one of shear loading. Consequently, multiple shear tests may be required to obtain the shear stress ratio along this curve. For anisotropic materials without tension-compression asymmetry, tests must be performed at orientations from Point ① to Point ②, and from Point ① to Point ③ for asymmetric materials such as magnesium alloys.

Although the constraint of Eq. (35) is trivial for the non-quadratic Hosford yield criterion, it is not trivial for anisotropic yield functions as demonstrated in Section 6.1 where the conventional method for yield function calibration can fail to satisfy this relation, resulting in the development of a non-physical hydrostatic stress in shear loading.
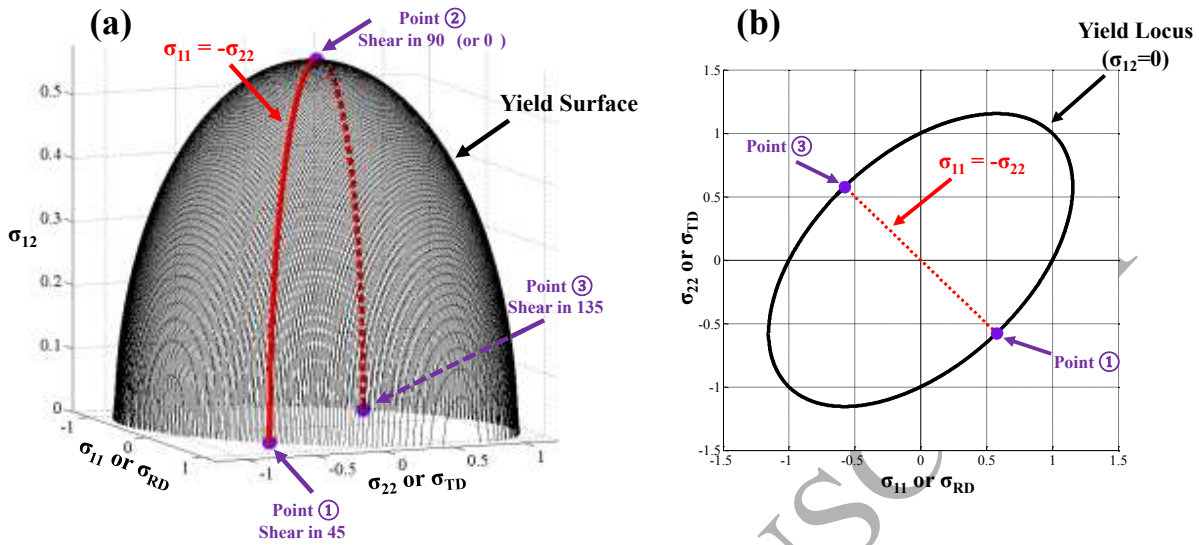
Figure 3 – von Mises yield function plotted (a) in σ_{11}-σ_{22}-σ_{12}-space, and (b) on the σ_{11}-σ_{22} plane when σ_{12}=0. Note that only the top half of the yield surface is depicted in Figure 3a and the red curve corresponds to zero hydrostatic stress, and based on Section 4, principal strains should be equal and opposite along this curve.

5. Experimental Data

5.1. Materials

Two different types of aluminum alloy sheet were considered in the present paper: (i) a highly-textured AA2090-T3 (Al-2.2Li-2.7Cu-0.12Zr) with a nominal thickness of 1.6 mm with the experimental results taken from Barlat *et al.* (2003), and (ii) AA7075-T6 (Al-6Zn-2.9Mg-2Cu-0.2Ti-0.3Mn-0.4Si-0.5Fe) with a nominal thickness of 2 mm with the characterization tests performed as part of the current research to obtain the constitutive plastic response of the material, as described in Section 5.2.

5.2. Constitutive Response

The experimental data for AA2090-T3 was published by Barlat *et al.* (2003) and the corresponding stress ratios and r-values are re-stated here, for reference, in Table 1. However, in-plane shear test results were not provided in Barlat *et al.* (2003). For this reason, a second aluminum alloy sheet (AA7075-T6) was also considered for the calibration of anisotropic yield

functions. Constitutive characterization for AA7075-T6 was performed in the present study and the results are presented in this section. It should be noted that all the experimental tests reported below were conducted at room temperature under a quasi-static strain rate of 0.001 s^{-1}.

Uniaxial tension tests were performed on the AA7075-T6 sheet using a sub-sized ASTM E8 dogbone specimen shown in Figure 4 tested in an MTS model 45 hydraulic tensile frame. For the AA7075-T6 experiments, stereo digital image correlation (DIC) techniques were used to obtain full-field strain measurements using two Point Grey 4.1 MP cameras with 180 mm (1:3.5) Tamron$^{®}$ lenses. The DIC images were recorded at a rate of 5 frames per second and analyzed using a subset size of 29 pixels, step size of 5 pixels and strain filter of 9 by the commercial VIC3D software package from Correlated Solutions Inc. To ensure the repeatability of the tests, at least five repeats were performed for each loading condition and material orientation while only the average values are reported in this paper.

Figure 5 shows the uniaxial tension true stress versus plastic work response of AA7075-T6 in the three orientations of RD, DD, and TD and the corresponding stress ratios are given in Table 1. Standard deviations of ±0.005, ±0.002, and ±0.007 were obtained for the uniaxial stress ratios in RD, DD, and TD, respectively. Furthermore, average r-values of 0.78, 0.95, and 1.34 were calculated for the orientations of RD, DD, and TD, with standard deviations of ±0.06, ±0.04, and ±0.10, respectively.
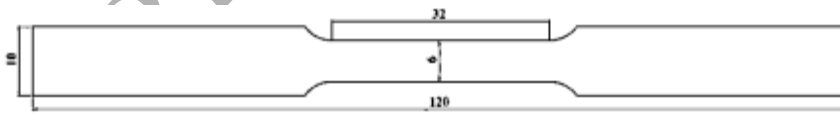

Figure 4 – Geometry of the uniaxial tensile specimen. All dimensions are in millimeters.
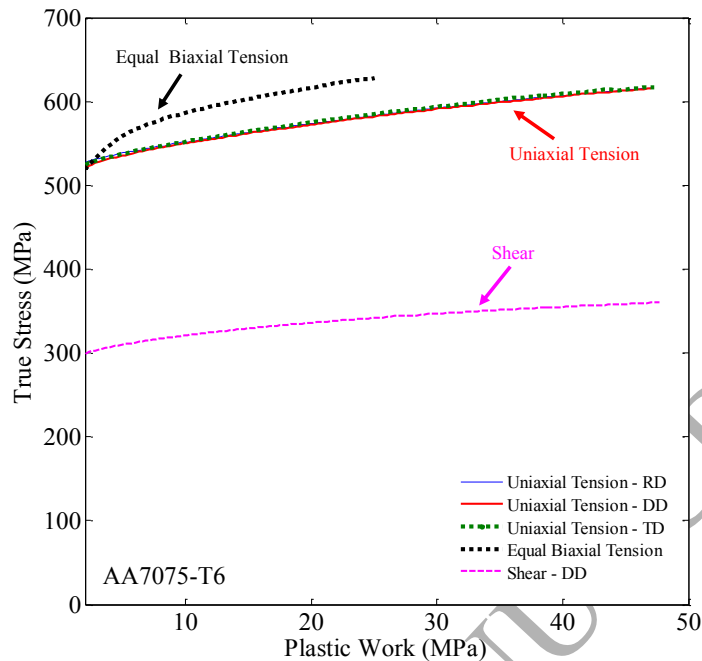
Figure 5 – Response of AA7075-T6 under different loading conditions.

The equal-biaxial tensile condition can be captured using through-thickness compression tests as explained by Barlat *et al.* (2003). The experimental methodology of Kurukuri *et al.* (2014) and Steglich *et al.* (2014) was followed where cubic specimens with aspect ratio of unity were fabricated by adhesively bonding six layers of sheets, as depicted in Figure 6 and the specimens were tested using a compression device shown in Figure 6. For sample preparation, the sheet layers were carefully cleaned using Acetone and then J-B-Weld® adhesive was applied between the inner layers. After curing the adhesive for 24 hours, the top and bottom surfaces (where the specimen contacts the upper and lower compression plates of the testing device) were polished to a mirror-finish. Furthermore, Teflon® spray was applied as lubricant to reduce friction between the specimens and the compression platens. An Instron model 1331 servo-hydraulic testing machine was used to apply the compressive force to the specimens. The flow stress response of the material is shown in Figure 5 and an equal-biaxial stress ratio of 1.057 and r-value of 0.88 with standard deviations of ±0.01 and ±0.06 were calculated, respectively.
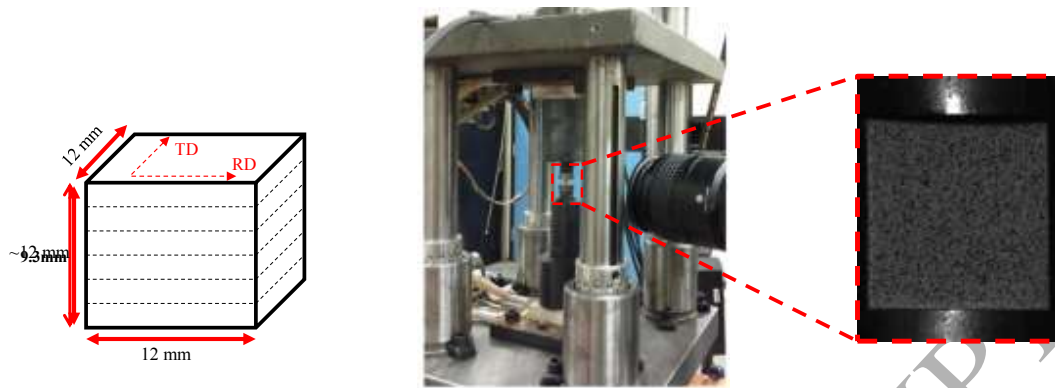
21

Figure 6 – Stacked compression specimen (left), compression testing device used to ensure alignment (center) and photograph of specimen showing speckle pattern for DIC-based strain measurement (right).

Shear tests were performed on the AA7075-T6 sheet using a shear specimen adopted from Peirs *et al.* (2012), shown in Figure 7. This specimen geometry was adopted since it is relatively simple to fabricate, does not require through-thickness machining, and provides a relatively uniform shear strain distribution. Recent work by Abedini *et al.* (2015, 2017a,b), and Rahmaan *et al.* (2017) has demonstrated the advantages of the Peirs *et al.* (2012) geometry for constitutive and fracture characterization of different sheet materials. The shear tests on AA7075-T6 were done with the applied load in the diagonal direction of the sheet which results in principal stresses in the rolling and transverse directions as explained in Section 4. The MTS hydraulic tensile frame was also used to apply loads to the shear specimen. The shear response of the material is shown in Figure 5 and a shear stress ratio (relative to the tensile flow stress in the RD) of 0.583 with a standard deviation of ±0.003 was calculated. A summary of the plastic constitutive response of AA7075-T6 is given in Table 1 in which the stress ratios belong to the plastic work level of 25 MPa (corresponding to 5% equivalent plastic strain in the uniaxial tension in RD). Note that as typically assumed in the literature (*e.g.* Barlat *et al.*, 2003; 2005; Yoon *et al.*, 2004) the shape of the calibrated yield criteria are assumed to be constant and independent of the level of plastic deformation. For this reason, the yield calibration performed at low strain levels where the simple shear test is valid and before the onset of necking in a tensile test can be applied to forming simulations where the strain levels are much larger.
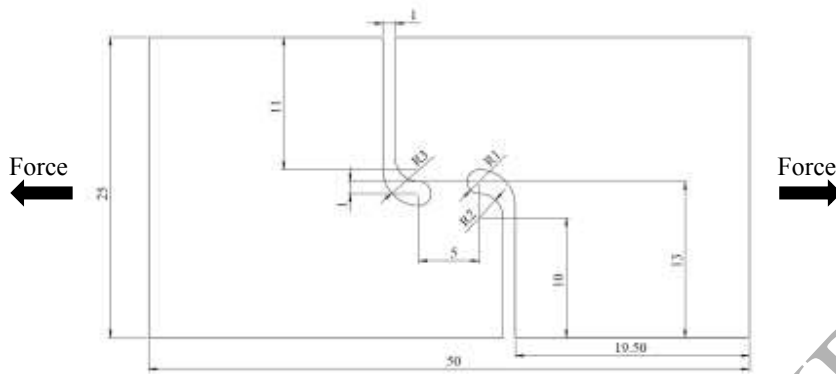
22

Figure 7 – Shear specimen geometry of Peirs *et al.* (2012). All dimensions are in millimeters.

Table 1 – Normalized yield stress and r-values for AA2090-T3 (Barlat *et al.*, 2003) and AA7075-T6. Stress ratios are with respect to uniaxial tensile yielding in the rolling direction

Material	σ_0	σ_{45}	σ_{90}	σ_b	τ_{45}	r_0	r_{45}	r_{90}	r_b
2090-T3	1.000	0.811	0.910	1.035	-	0.21	1.58	0.69	0.67
7075-T6	1.000	0.998	1.003	1.057	0.582	0.78	0.95	1.34	0.88

6. Results and Comparison

6.1. Calibrations with the Conventional Method

As explained in Section 3, the conventional method of calibration is commonly used to determine the coefficients of anisotropic yield functions including the Yld2000-2d model. For the purposes of the subsequent discussions, for the AA2090-T3 alloy, the coefficients reported by Barlat *et al.* (2003) for Yld2000-2d were used (Table 2). Note that the conventional calibration was used in Barlat *et al.* (2003) with the weighting values of w_σ =1.0 and w_r =0.1 to determine the anisotropy coefficients. Moreover, the coefficients of the Yld2000-2d yield function were calibrated for the AA7075-T6 alloy in the present study using the GA optimization method described in Section 3 with the experimental data reported in Table 1 (uniaxial and equal-biaxial tensile yield stress and r-values and shear yield stress), and the corresponding coefficients are given in Table 2. For both alloys, an exponent of *a*=8 was used for the anisotropic model as recommended for fcc materials (Barlat *et al.*, 2003). Figures 8 and 9 show

23

the yield loci plotted using the coefficients of Table 2 for AA2090-T3 and AA7075-T6, respectively. Moreover, the r-values and stress ratios for uniaxial tension tests with different orientations are also plotted along with the experimental data used for calibrations. Also the values of *Error* in Eq. (18) are presented in Table 3 for the two materials. It can be seen that the Yld2000-2d model matches the experimental data with good accuracy. However, it will be shown that predictions of the models calibrated with the conventional method are inconsistent with the mechanics of shear deformation described in Section 4.

Table 2 – Coefficients of the Yld2000-2d calibrated with the conventional method.

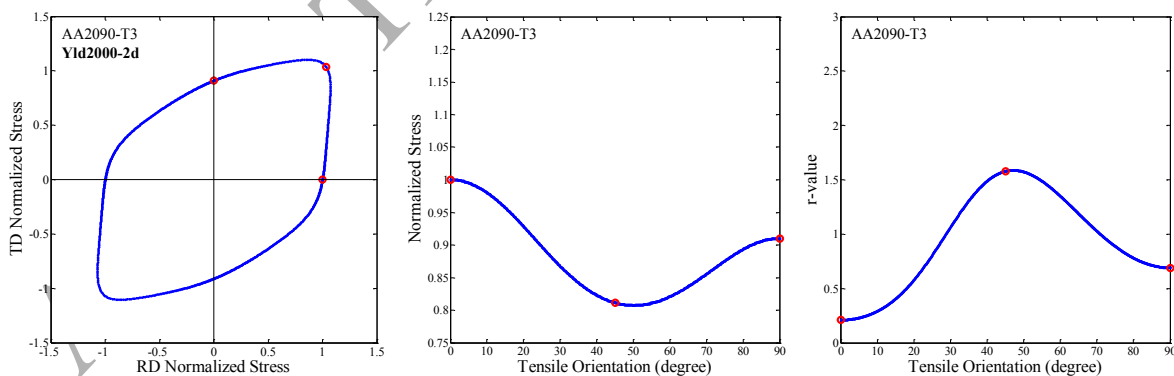| Yld2000-2d		
Coefficient	2090-T3 (Barlat *et al.*, 2003)	7075-T6
α_1	0.4865	1.5526
α_2	1.3783	-1.5341
α_3	0.7536	-0.1921
α_4	1.0246	0.7845
α_5	1.0363	0.8600
α_6	0.9036	0.1695
α_7	1.2321	0.2948
α_8	1.4858	1.6278
a	8.00	8.00

Figure 8 – Yield locus, tensile stress ratios and r-values of Yld2000-2d for AA2090-T3 calibrated with the conventional method with the coefficients taken from Barlat *et al.* (2003). Red circles show the experimental results.
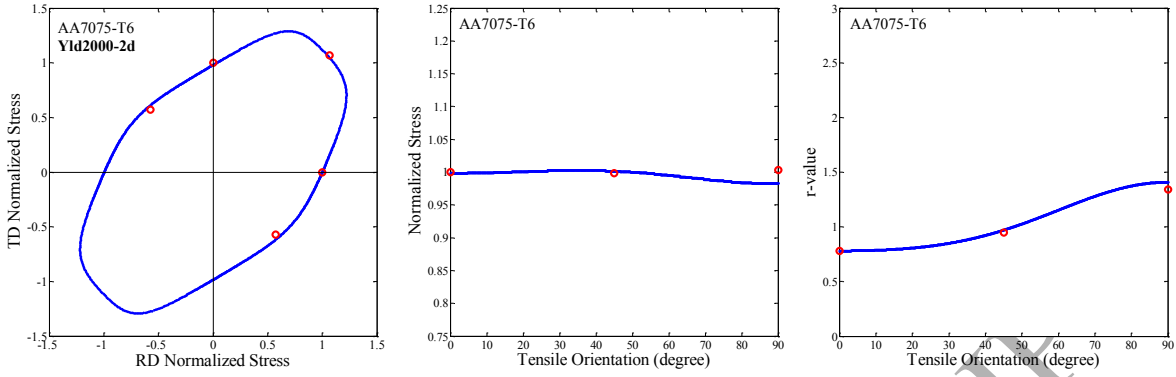
24

Figure 9 – Yield locus, tensile stress ratios and r-values of Yld2000-2d for AA7075-T6 calibrated with the conventional method. Red circles show the experimental results.

Table 3 – Values of *Error* in Eq. (18) along with its components,

Materials	$w_\sigma \sum_{i=1}^{m} \left(\left(\dfrac{\sigma_{model}}{\sigma_{exp}} \right)_i - 1 \right)^2$	$w_r \sum_{i=1}^{m} \left(\left(\dfrac{r_{model}}{r_{exp}} \right)_i - 1 \right)^2$	*Error*
2090-T3	$3.7(10^{-6})$	$2.9(10^{-6})$	$6.6(10^{-6})$
7075-T6	$4.5(10^{-4})$	$3.4(10^{-4})$	$7.9(10^{-4})$

The stress triaxiality is a measure of the severity of the hydrostatic stress and is widely used in fracture characterization of materials (*e.g.* Bai and Wierzbicki, 2008; Dunand and Mohr, 2011; Abedini *et al.*, 2017a). The stress triaxiality, η, is defined as:

$$\eta = \frac{\sigma_{hyd}}{\sigma_{eq}} \tag{41}$$

In plane-stress loading, the stress state can be uniquely defined using only the stress triaxiality. For the plane-stress condition and proportional loading defined by constant principal stress ratios, ρ, the stress triaxiality can be determined for the calibrated yield criterion using:

$$\eta = \frac{(\rho + 1)\, \sigma_1}{\sigma_{eq}} \quad , \quad \rho = \frac{\sigma_2}{\sigma_1} \tag{42,43}$$

The ratio of principal strain increments can be calculated as a function of ρ by using Eq. (2). For a simple yield criterion such as the von Mises model, closed-form solutions can be obtained for

the relationship between the strain ratio and stress triaxiality (Abedini *et al.*, 2017a); however, for general anisotropic yield criteria, as in the present work, these values should be calculated numerically which is relatively straightforward for a given stress ratio and calibrated constitutive model.

Assuming associated flow for both aluminum alloys, the stress triaxialities were calculated with respect to the principal strain ratios ($\varepsilon_2/\varepsilon_1$) for the yield loci shown in Figures 8 and 9 for the range of stress states from shear to equal-biaxial tension. Two different regions (regions #1 and #2) are defined in Figure 10 for the locations where the stress triaxialities are investigated. The variations of the stress triaxiality with respect to the principal strain ratios are shown in Figures 11 and 12 for AA2090-T3 and AA7075-T6, respectively. Similar curves are also shown by setting all the coefficients of the anisotropic yield function to unity, reducing it to the Hosford isotropic model with an exponent of $a= 8.0$ (Hosford, 1972).
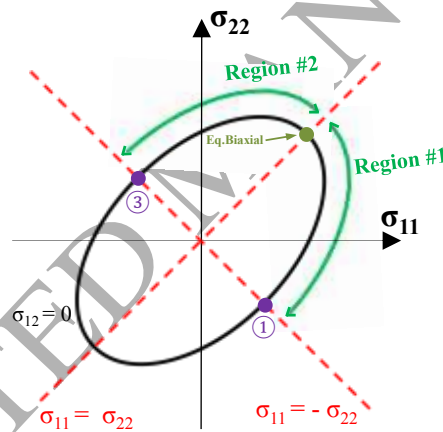

Figure 10 – Labels and locations of the regions where stress triaxialities are investigated in the x_1-x_2 or RD-TD plane. As explained in Section 4, Point ① corresponds to shear test with the applied load in the 45° orientation and Point ② corresponds to shear test with the applied load in the 135° orientation. Note that the regions illustrated in the figure belong to a yield function at a fixed plastic work level.

Emphasis is placed on the shear points in Figures 11 and 12 as indicated with the labels ① and ③ (corresponding to the naming convention of Figure 3), in which, as discussed in Section 4, the stress triaxialities are zero due to the hydrostatic stress of zero (*i.e.* $\eta=0$), and the principal strain ratios are supposed to be equal to -1 (*i.e.* $\xi=-1$). However, as opposed to the isotropic case, this condition is not satisfied for the anisotropic models calibrated with the conventional method.

26

It should also be noted that the shift in the equal-biaxial points between the isotropic Hosford and anisotropic yield criteria is due to a value of the equal-biaxial r-value that is non-unity.

Furthermore, in order to evaluate shear states in other in-plane directions, principal strain ratios were calculated for the shear points along the $\sigma_{11}=-\sigma_{22}$ curve (from Point ① to ② in Figure 3a), and the results are presented in Figure 13. Note that the principal strain ratios from Point ② to ③ (see Figure 3a) are the inverse of the values from Point ① to ② and are not shown here for brevity. It can be seen from Figure 13 that the anisotropic models predict principal strain ratios other than the desired value of $\xi=-1$ along the $\sigma_{11}=-\sigma_{22}$ curve except for Point ② for which the strain ratio of -1 is achieved due to the fact that the normal vector, $\dfrac{\partial\Phi}{\partial\boldsymbol{\sigma}}$, is parallel to the σ_{12} direction and therefore, no normal strain components are predicted at this point. The deviations of the principal strain ratios from the desired value of $\xi=-1$ are the highest at the location of Point ① and they continuously decrease towards Point ②.
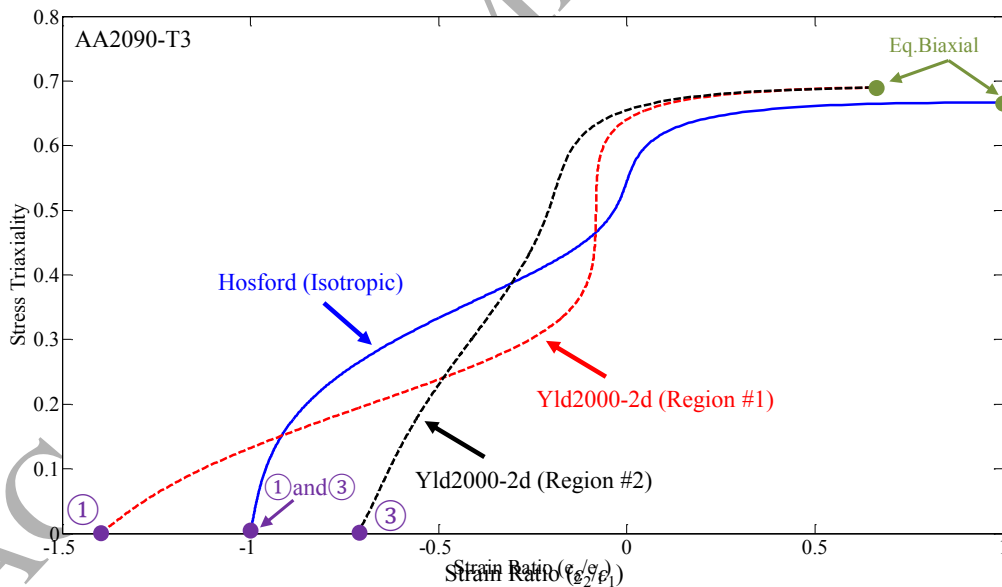

Figure 11 – Stress triaxiality vs. strain ratios of Yld2000-2d for AA2090-T3 in x_1-x_2 or RD-TD plane in the plane-stress condition. The coefficients of Yld2000-2d were taken from Barlat *et al.* (2003). Only the isotropic Hosford criterion leads to stress triaxiality of zero at strain ratio of -1.
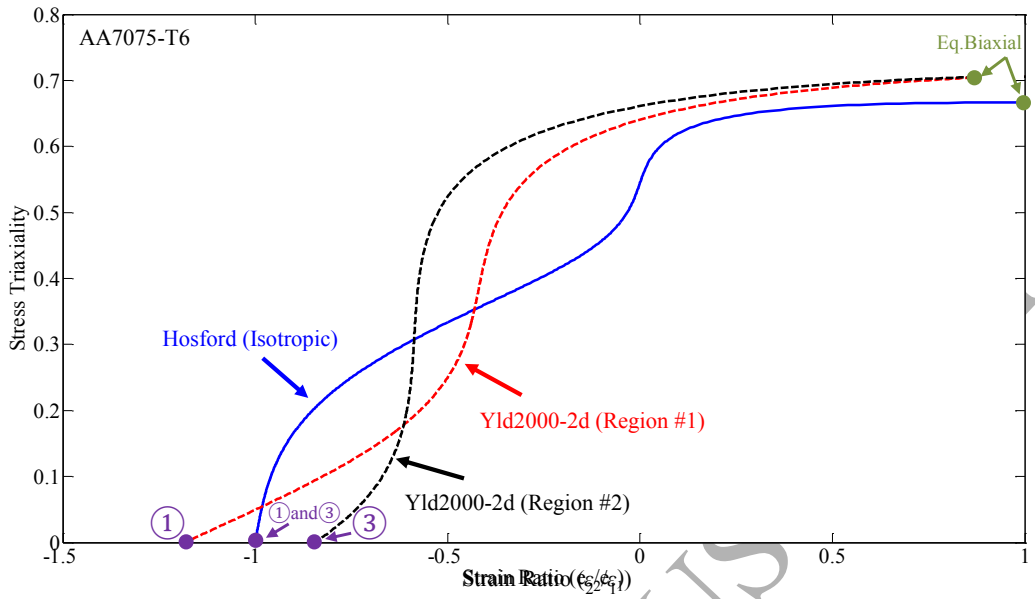
27

Figure 12 – Stress triaxiality vs. strain ratios of Yld2000-2d for AA7075-T6 in x_1-x_2 or RD-TD plane in the plan-stress condition. Only the isotropic Hosford criterion leads to stress triaxiality of zero at strain ratio of -1.
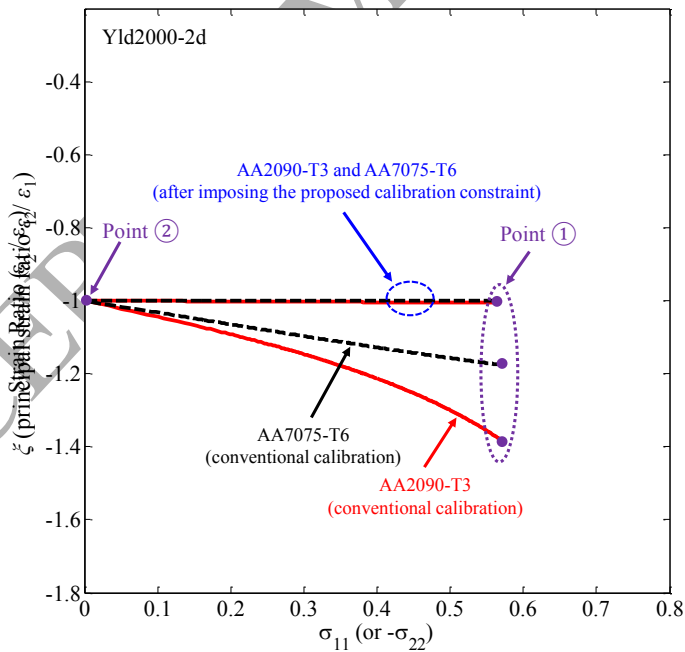

Figure 13 – Principal strain ratios along the σ_{11}=- σ_{22} curve for the Yld2000-2d anisotropic yield function using the different calibrations approaches. Note that σ_{11}, σ_{22}, and σ_{12} change along the σ_{11}=- σ_{22} curve.

It is important to mention that in shear simulations with displacement-based boundary conditions, a principal strain relation of $d\varepsilon_1 = -d\varepsilon_2$ is always achieved as explained in Section 4.1 and shown in detail by Rahmaan *et al.* (2017) due to the imposed deformation gradient of Eq. (19). The results of Figures 11-13 show that for the calibrated anisotropic models, the principal strains are not equal and opposite (*i.e.* $d\varepsilon_1 \neq -d\varepsilon_2$ or $\xi \neq -1$) along the $\sigma_{11} = -\sigma_{22}$ curve along which the hydrostatic stress is zero; therefore, the use of the yield loci depicted in Figures 8 and 9 for simulations involving shear, will result in an abnormal, non-zero hydrostatic stress (*i.e.* $\eta \neq 0$) that is undesired in a shear loading condition, as explained in Section 4.

Furthermore, if a stress-based boundary condition is applied in shear simulations to ensure that a zero hydrostatic stress is achieved, the resulting principal strains would not satisfy $\xi = -1$, which is in contradiction with the definition of the shear loading (Section 4) as well as experimental observations (Figure 2). The results of Figures 11-13 show that additional calibration constraints are required to adjust or correct calibration of anisotropic yield functions in shear regions.

6.2. Calibrations with a Proposed Shear Constraint on the Flow Rule

The results of Section 6.1 showed that shear regions of the anisotropic yield criterion calibrated with the conventional method do not satisfy the necessary shear condition of zero hydrostatic stress at the principal strain ratio of -1. In other words, the hydrostatic stress is not zero where the principal strain ratio is equal to -1 and, conversely, the principal strain ratio is not equal to -1 where the hydrostatic stress is equal to zero. To address this issue, a new calibration constraint was introduced into the optimization scheme to enforce the requirement that $\xi = -1$:

$$Error = w_\sigma \sum_{i=1}^{m} \left(\left(\frac{\sigma_{\text{model}}}{\sigma_{\text{exp}}} \right)_i - 1 \right)^2 + w_r \sum_{i=1}^{m} \left(\left(\frac{r_{\text{model}}}{r_{\text{exp}}} \right)_i - 1 \right)^2 + w_\xi \left(\left(\frac{\xi_{\text{model}}}{-1} \right) - 1 \right)^2 \qquad (44)$$

where ξ_{model} is the predicted ratio of principal strains at Point ① and w_ξ is a weighting value of the new calibration constraint. Thus, the new term in Eq. (44) enforces the principal strain ratio to be equal to -1 at Point ① (where the highest deviation from $\xi = -1$ is observed for shear regions of anisotropic models calibrated with the conventional method, see Figure 13). Note that the new calibration constraint can alternatively be imposed on Point ③ since its principal strain ratio is

the inverse of Points ① (see Figures 11 and 12), and adjusting the principal strain ratio of either Point ① or ③ will automatically correct the principal strain ratio for the other point as well.

The calibration of the anisotropic Yld2000-2d yield function was performed again with the same set of experimental data (Table 1) but this time Eq. (44) was used with the weighting values of $w_\sigma = 1.0$, $w_r = 0.1$, and $w_\xi = 1.0$. Note that, in order to better demonstrate the influence of the proposed constraint, a large weighting value was selected for w_ξ. The coefficients of the anisotropic yield function are reported in Table 4 and their corresponding predictions are shown in Figures 14 and 15 for AA2090-T3 and AA7075-T6, respectively. Also the values of *Error* in Eq. (44) are presented in Table 5 for the two materials. Furthermore, Table 6 compares experimental data with the predictions of anisotropic yield functions calibrated with the two approaches for different stress states. It can be seen from Figures 14 and 15 and Tables 5 and 6 that compared to the experimental results, the agreement between the yield functions calibrated with the proposed method and measured values is good although compared to the conventional calibrations some degree of accuracy has been lost in the uniaxial and biaxial regions. This lower agreement in the first quadrant is not unexpected due to the addition of the new shear constraint to calibrate the yield function. In other words, with the addition of the new constraint, the flexibility of the yield surface is reduced but it will be shown that its physical foundation is improved in shear loading. To restore the desired accuracy in the first quadrant, an alternate yield function with more calibration parameters can be adopted or a non-associated flow rule can be used as discussed in Section 7.

Table 4 – Coefficients of Yld2000-2d calibrated with the proposed shear constraint.

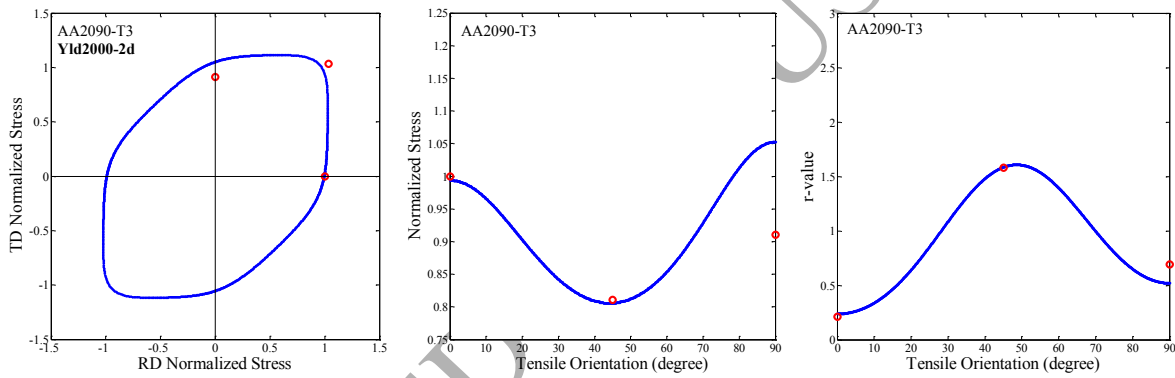| Yld2000-2d		
Coefficient	**2090-T3**	**7075-T6**
α_1	0.8603	0.9506
α_2	0.9292	0.9922
α_3	0.9573	0.9026
α_4	0.9768	0.9361
α_5	1.0634	0.9752
α_6	1.0389	0.8157
α_7	-1.2505	0.9821
α_8	1.4496	1.1010
a	8.00	8.00

Figure 14 – Yield locus, tensile stress ratios and r-values of Yld2000-2d for AA2090-T3 calibrated with the proposed shear constraint. Red circles show the experimental results.
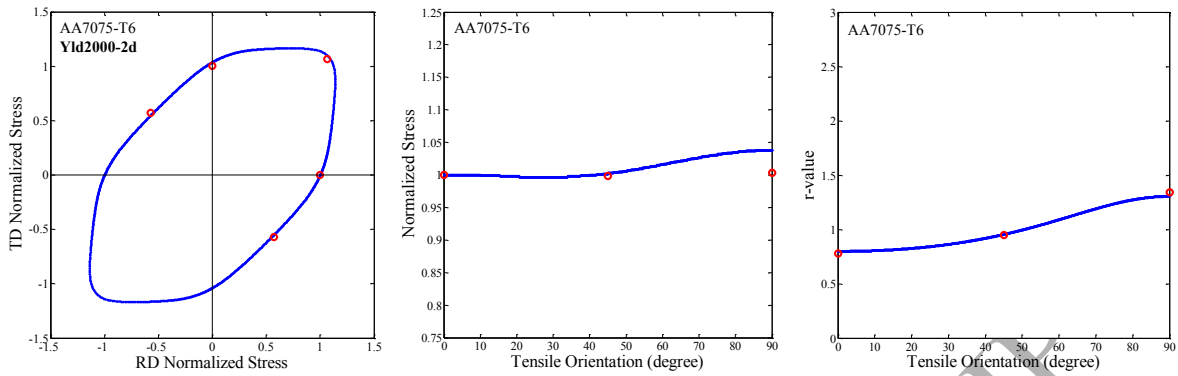
Figure 15 – Yield locus, tensile stress ratios and r-values of Yld2000-2d for AA7075-T6 calibrated with the proposed shear constraint. Red circles show the experimental results. The yield function was calibrated at the plastic work level of 25 MPa corresponding to an equivalent plastic strain of 5% for uniaxial tension in RD.

Table 5 – Values of *Error* in Eq. (44) along with its components,

Materials	$w_\sigma \sum_{i=1}^{m} \left(\left(\frac{\sigma_{model}}{\sigma_{exp}} \right)_i - 1 \right)^2$	$w_r \sum_{i=1}^{m} \left(\left(\frac{r_{model}}{r_{exp}} \right)_i - 1 \right)^2$	$w_\xi \left(\left(\frac{\xi_{model}}{-1} \right) - 1 \right)^2$	*Error*
2090-T3	$2.7(10^{-2})$	$1.5(10^{-2})$	$5.2(10^{-5})$	$4.2(10^{-2})$
7075-T6	$1.9(10^{-3})$	$2.0(10^{-4})$	$1.5(10^{-7})$	$2.1(10^{-3})$

32

Table 6 – Comparison between experimental data and predictions of yield functions for different stress states for AA2090-T3 and AA7075-T6.

Stress State	AA2090-T3			AA7075-T6		
	Experiment	Conventional Calibration	Proposed Calibration	Experiment	Conventional Calibration	Proposed Calibration
Uniaxial Tension RD: Stress Ratio (r-value)	1.000 (0.21)	1.000 (0.21)	1.000 (0.23)	1.000 (0.78)	1.000 (0.78)	1.000 (0.80)
Uniaxial Tension DD Stress Ratio (r-value)	0.811 (1.58)	0.811 (1.58)	0.806 (1.59)	0.998 (0.95)	1.001 (0.97)	1.002 (0.96)
Uniaxial Tension TD Stress Ratio (r-value)	0.910 (0.69)	0.910 (0.69)	1.053 (0.52)	1.003 (1.34)	0.984 (1.41)	1.038 (1.31)
Equal-Biaxial Tension Stress Ratio (r-value)	1.035 (0.67)	1.035 (0.67)	0.982 (0.59)	1.057 (0.88)	1.055 (0.88)	1.060 (0.86)
Shear in DD Stress Ratio	-	0.580	0.607	0.582	0.596	0.570
Shear in RD Stress Ratio	-	0.441	0.435	-	0.614	0.555
Plane-strain Tension RD Stress Ratio	-	1.072	1.026	-	1.219	1.139
Plane-strain Tension TD Stress Ratio	-	1.102	1.115	-	1.292	1.167

Figure 16 compares yield loci of AA7075-T6 calibrated with the conventional and proposed approaches. This figure demonstrates that for AA7075-T6, calibration with the proposed method reduces the overshoot in stress in the plane-strain region of the locus. Further evaluation of this behaviour would require plane-strain experiments and will be addressed in future work.
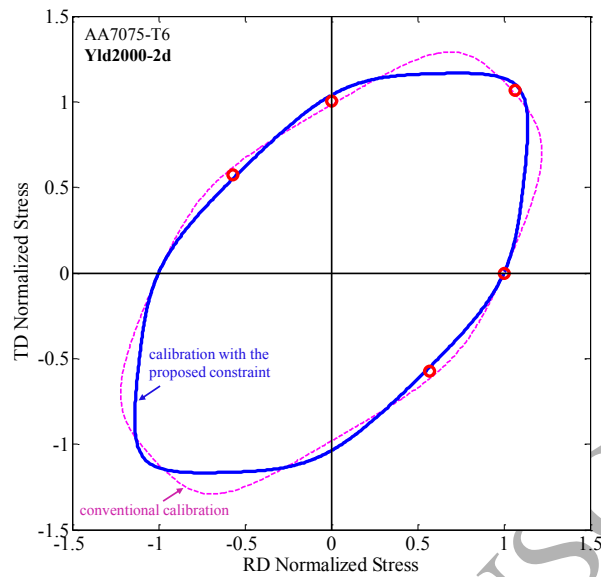
Figure 16 – Yield loci for AA7075-T6 calibrated with the conventional and proposed methods. Note that the addition of the proposed shear constraints may result in some accuracy loss in non-shear stress states.

Stress triaxialities with respect to the principal strain ratios were also calculated using the same approach described in Section 6.1 and the results are plotted in Figures 17 and 18 for AA2090-T3 and AA7075-T6, respectively. It can be seen that after the addition of the new shear constraint, the anomalous predictions in the shear regions are resolved, as demonstrated by the stress triaxialities becoming zero at the principal strain ratio of -1. Furthermore, the principal strain ratios were also plotted along the $\sigma_{11}=-\sigma_{22}$ or zero hydrostatic stress curve and the results are shown in Figure 13. As expected, the new calibration approach enforces the principal strain ratios to be equal to -1 at Point ① and this automatically corrects the principal strain ratios of the other shear points along the $\sigma_{11}=-\sigma_{22}$ curve. This guarantees that by introducing the shear calibration constraint in the calibration procedure, as proposed in this paper, no hydrostatic stress will be predicted in the shear loading condition. This response will be further examined in Section 6.3.
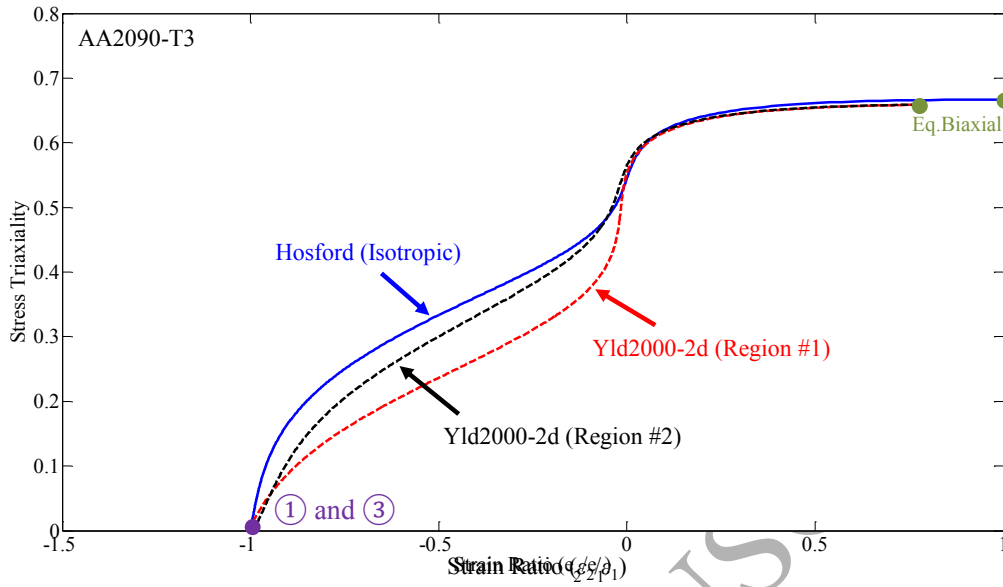
Figure 17 – Stress triaxiality vs. strain ratios of Yld2000-2d for AA2090-T3 in x_1-x_2 or RD-TD plane in the plane-stress condition. The proposed shear constraint was used for calibrations.
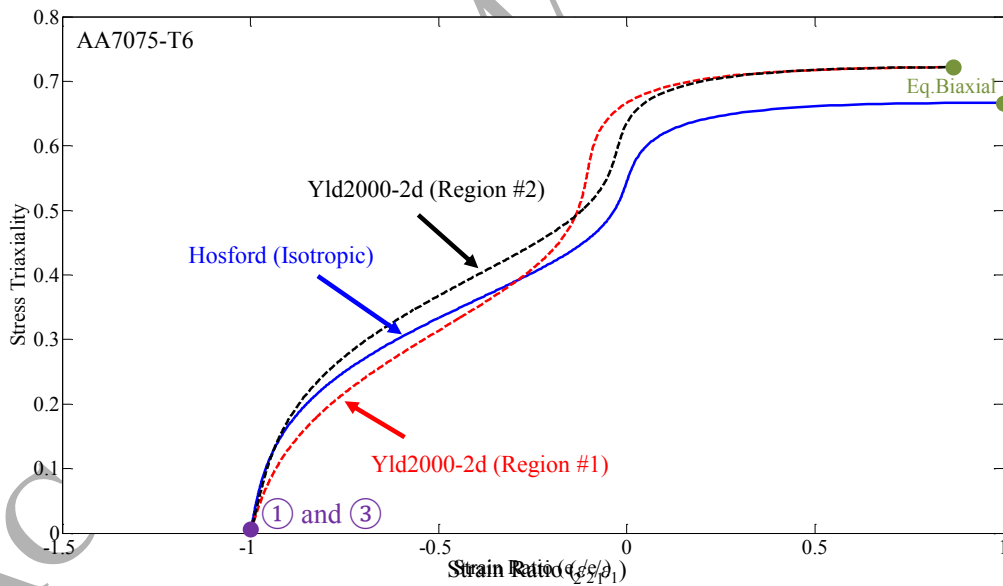

Figure 18 – Stress triaxiality vs. strain ratios of Yld2000-2d for AA7075-T6 in x_1-x_2 or RD-TD plane in the plane-stress condition. The proposed shear constraint was used for calibrations.

6.3. Single Element Simulations

In order to better show the issues that may arise using the anisotropy coefficients calibrated with the conventional method, single element simulations were performed using the commercial FE code, LS-DYNA. A single shell element was modelled under a simple shear loading condition (see Figure 1) and the Yld2000-2d model available in LS-DYNA (*MAT_BARLAT_YLD2000) was employed using the anisotropy coefficients of Table 2. Furthermore, the anisotropy coefficients in Table 4 based on the calibrations using the proposed shear constraint were also considered for comparison. Figure 19 shows the evolution of the stress triaxiality with respect to the plastic strain for AA2090-T3 and AA7075-T6. The shear states targeted are Points ① and ③ (Note that as explained in Section 6.1, the stress state deviates from the locations of these points if $\xi \neq -1$). It can be observed that, using the anisotropy coefficients calibrated with the conventional method result in anomalous stress triaxialities with absolute values of approximately ±0.13 and ±0.05 for AA2090-T3 and AA7075-T6, respectively, while the stress triaxialities are negligibly small using the coefficients calibrated with the proposed constraint. Note that it is possible to increase the value of w_ξ in Eq. (44) to completely eliminate the hydrostatic stress at a cost of less accuracy in other states due to the limited flexibility of the yield function with the associated flow rule. It is important to mention that the stress triaxiality of Point ① becomes positive (tensile loading) while Point ③ results in a negative hydrostatic stress (compressive loading). Also the stress triaxiality of Point ③ has the opposite sign to the values of Point ①.
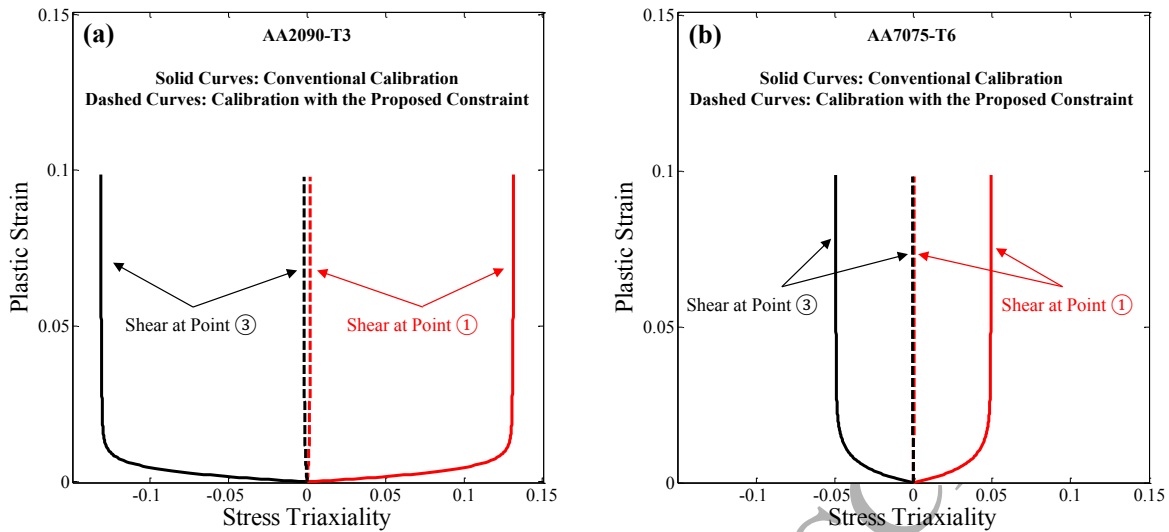
Figure 19 –Stress triaxiality vs. plastic strain obtained with single element simulations in shear using Yld2000-2d for (a) AA2090-T3 and (b) AA7075-T6.

7. Discussion

7. 1. Influence of the Proposed Constraint on Forming Simulations

The analyses in Section 6.3 were based on single element simulations to focus solely on the role of anisotropic models on the shear state; however, accurate prediction of yield functions with the proposed shear constraint can have significant influence on large-scale forming and crashworthiness simulations of models with shear-dominated stress states. For instance, in cup drawing (Harpell *et al.*, 2000; Ghaffari Tari and Worswick, 2015), different regions of the blank are subjected to different stress states, but the majority of the plastic flow occurs in the flange region where the stress consists of tangential compressive and radial tensile components; such stress states lie in the second and fourth quadrants of the yield locus with in-plane shear loading. Therefore, accurate numerical predictions under shear or near-shear states in terms of strain path and stress components should lead to more accurate predictions of drawing behaviour.

7. 2. Influence of the Proposed Constraint on Fracture Predictions

The work presented herein has demonstrated that the conventional calibration method can result in inaccurate prediction of stress-state (triaxiality) under shear loading. Such errors in predicted triaxiality can have major ramifications on phenomenological fracture modelling of materials, for example, using the popular MMC-type equations (Bai and Wierzbicki, 2008; 2010). Such uncoupled fracture approaches are normally calibrated using the correct assumption that stress triaxiality is zero for a shear stress state whereas finite element models utilizing anisotropic yield functions calibrated with the conventional method will predict non-zero stress triaxialities that may have significant impact on fracture predictions. To illustrate this potential effect on fracture prediction, a phenomenological fracture locus for an aluminum alloy was taken from Bai and Wierzbicki (2008) and its corresponding fracture strains versus stress triaxiality are plotted in Figure 20. The current work has demonstrated that stress triaxiality under shear loading can be ±0.13 using the conventional calibration method (Figure 19) instead of zero. For such an erroneous triaxiality level, the predicted failure strain (Figure 20) becomes 0.26 for a stress triaxiality of 0.13 and 0.24 for a stress triaxiality of -0.13 instead of 0.21 for a triaxiality of zero, an error of up to approximately 20%. The proposed calibration method enforces zero triaxiality under shear loading, thus avoiding this error.
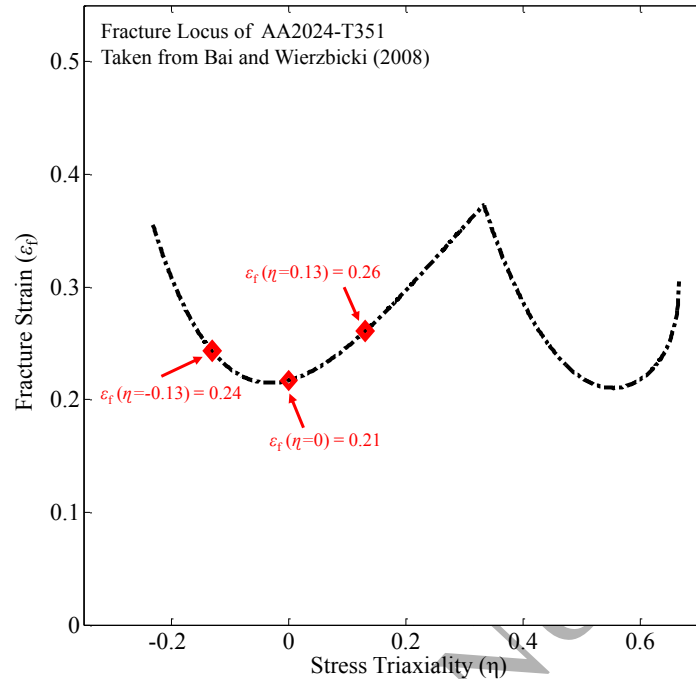
38

Figure 20 – Fracture locus of AA2024-T351 taken from Bai and Wierzbicki (2008) showing the influence of stress triaxiality on fracture strain.

7. 3. Applicability of the Proposed Constraint to General 3-D Conditions

It should be mentioned that the improvement in predicted strain ratios, seen in Figure 13, when the proposed shear constraint was applied to the plane-stress Yld2000-2d model, will not necessarily hold for all anisotropic yield functions. For example, the principal strain ratios under shear states obtained using the three-dimensional Yld2004-18p anisotropic yield function for general stress states (Barlat *et al.,* 2005) were also examined. Specifically, shear prediction using the anisotropy coefficients reported by Barlat *et al.* (2005) for AA2090-T3 were compared with those obtained after imposing the proposed calibration constraint, as shown in Figure 21. The strain ratios under shear loading obtained using the conventional calibration drift from the correct value of -1, whereas those using the new calibration constraint are much closer to this value. It can also be seen that compared to the results of the conventional calibration, the proposed calibration method improves the predictions of the principal strain ratios in shear to be in closer agreement with ξ=-1; however, the slight deviation of the curve from a value of -1

39

suggests that a more sophisticated treatment may be required to correct the yield function calibration in the shear region of yield functions with 3-D formulations. For example, it might be required to enforce the condition that $d\varepsilon_1 = -d\varepsilon_2$ all along the $\sigma_{11} = -\sigma_{22}$ curve, as opposed to the case in the present paper with the Yld2000-2d in which enforcing the shear constraint at just Point ① sufficed to correct the strain ratios for all shear states.
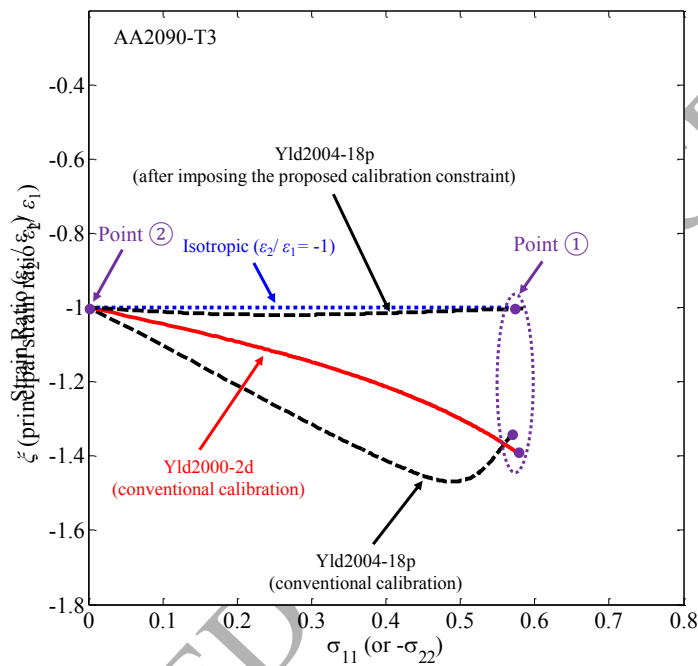

Figure 21 – Principal strain ratios along the $\sigma_{11} = -\sigma_{22}$ curve for the Yld2000-2d and Yld2004-18p anisotropic yield functions for AA2090-T3 with anisotropy coefficients calibrated with the conventional method, reported in Barlat *et al*. (2003) and Barlat *et al*. (2005), respectively. The results with the proposed calibration constraint on Yld2004-18p have also been plotted for comparison.

7. 4. Applicability of the Proposed Constraint to Non-associated Flow Rule

Although the new calibration approach is based on a physically necessary constraint, the trade-off in its adoption is potentially losing accuracy in other stress state regions as explained in Section 6.2. This effect can be exacerbated for the case of anisotropic yield functions that have a limited degree of flexibility for which the additional shear constraint may make the yield function over-constrained. This is an interesting result since the enforcement of these additional

shear constraints may favour use of a non-associated flow rule or adoption of additional linear transformations for increased flexibility. Using the non-associated flow rule, it is not required for yield functions to satisfy the new normality constraint imposed in the present paper since the normal vectors are calculated from a flow potential that can be calibrated independently from the yield function (Stoughton, 2002). To illustrate this, the Yld2000-2d model was re-calibrated utilizing a non-associated flow rule thereby allowing the yield function and plastic potential to be determined separately for AA2090-T3; the results are shown in Figure 22. The proposed shear calibration constraint was applied to the plastic potential; therefore, the yield function is able to capture the experimental yield points more accurately.
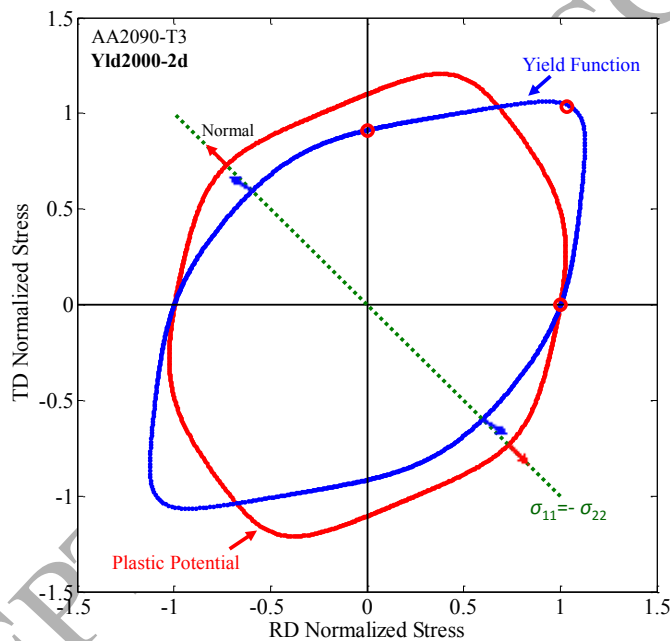

Figure 22 – Yield function and plastic potential of AA2090-T3 model calibrated utilizing a non-associated flow rule assumption. The proposed shear calibration constraint needs to be imposed on the plastic potential only.

An alternative option to account for the shear constraint could involve placing constraints upon the form of the linear transformations used to generalize an isotropic yield function to an anisotropic yield criterion as was done in Barlat family of yield criteria to ensure plastic incompressibility (Barlat and Lian, 1989; Barlat *et al.*, 1991; 1997; 2003; 2005). This

methodology would ensure that the shear constraint is automatically satisfied without requiring an explicit treatment to enforce it during calibration and provides an opportunity to develop new forms for anisotropic yield criteria in future work.

8. Conclusions

It was shown theoretically and using single element FE simulations that using the conventional method of calibrating the Yld2000-2d anisotropic yield function with only uniaxial tension and equal-biaxial tension data may result in abnormal predictions with non-zero stress triaxiality in the shear region. This non-physical artefact may have important ramifications for phenomenological fracture modelling using a MMC-type approach. To overcome this issue, a physically necessary calibration constraint was proposed to enforce the principal strain to be equal and opposite at the location of shear regions of anisotropic yield functions. This necessary constraint is required to enforce physically-admissible shear stress states. Imposing the proposed shear constraint on the plastic potential resulted in correcting these artefacts with the expected reduction in the accuracy of the yield function in other regions of the yield surface. It was shown that the loss of accuracy can be eliminated by adopting yield functions with more flexibility or non-associated flow rules.

Acknowledgments

References

Abedini A, Butcher C, Anderson D, Worswick M J, Skszek T, Fracture characterization of automotive alloys in shear loading, SAE International Journal of Materials and Manufacturing, 2015, 8(3).

Abedini A, Butcher C, Worswick M J, Fracture characterization of rolled sheet alloys in shear loading: studies of specimen geometry, anisotropy, and rate sensitivity, Journal of Experimental Mechanics, 2017a, 57:75-88.

Abedini A, Butcher C, Nemcko M J, Kurukuri S, Worswick M J, Constitutive characterization of a rare-earth magnesium alloy sheet (ZEK100-O) in shear loading: studies of anisotropy and rate sensitivity, International Journal of Mechanical Sciences, 2017b, 128-129:54-69.

Abedrabbo N, Pourboghrat F, Carsley J, Forming of AA5182-O and AA5754-O at elevated temperatures using coupled thermo-mechanical finite element models, International Journal of Plasticity, 2007, 23:841-875.

Bai Y, Wierzbicki T, A new model of metal plasticity and fracture with pressure and Lode dependence, International Journal of Plasticity, 2008, 24:1071-1096.

Bai Y, Wierzbicki T, Application of extended Mohr-Coulomb criterion to ductile fracture, International Journal of Fracture, 2010, 161:1-20.

Banabic D, Barlat F, Cazacu O, Kuwabara T, Advances in anisotropy and formability, International Journal of Material Forming, 2010, 3:165-189.

Barlat F, Lian K, Plastic behavior and stretchability of sheet metals. Part I: a yield function for orthotropic sheets under plane stress conditions, International Journal of Plasticity, 1989, 5:51-66.

Barlat F, Lege D J, Brem J C, A 6-component yield function for anisotropic materials, International Journal of Plasticity, 1991, 7:693-712.

Barlat F, Maeda Y, Chung K, Yanagawa M, Brem J C, Hayashida Y, Lege D J, Matsui K, Murtha S J, Hattori S, Becker R C, Makosey S, Yield function development for aluminum alloy sheets, Journal of Mechanical Physics and Solids, 1997, 45:1727-1763.

Barlat F, Brem J C, Yoon J W, Chung K, Dick R E, Lege D J, Pourboghrat F, Choi S H, Chu E, Plane stress yield function for aluminum alloy sheets – part I: theory, International Journal of Plasticity, 2003, 21:1009-1039.

Barlat F, Aretz H, Yoon J W, Karabin M E, Brem J C, Dick R E, Linear transformation-based anisotropic yield functions, International Journal of Plasticity, 2005, 21:1009-1039.

Cai Z, Diao K, Wu X, Wan M, Constitutive modeling of evolving plasticity in high strength steel sheets, International Journal of Mechanical Sciences, 2016, 107:43-57.

Cazacu O, Revil-Baudard B, Barlat F, New interpretation of monotonic Swift effects: role of trension-compression asymmetry, Mechanics of Materials, 2013, 57:42-52.

Cvitanic V, Vlak F, Lozina Z, A finite element formulation based on non-associated plasticity for sheet metal forming, International Journal of Plasticity, 2008, 24:646-687.

Dunand M, Mohr D, Hybrid experimental-numerical analysis of basic ductile fracture experiments for sheet metals, International Journal of Solids and Structures, 2010, 47:1130-1143.

Dunand M, Mohr D, Optimized butterfly specimen for the fracture testing of sheet materials under combined normal and shear loading, Engineering Fracture Mechanics, 2011, 78:2919-2934.

Fourmeau M, Borvik T, Benallal A, Lademo O G, Hopperstad O S, On the plastic anisotropy of an aluminum alloy and its influence on the constrained multiaxial flow, International Journal of Plasticity, 2011, 27:2005-2025.

Fu J, Barlat F, Kim J H, Pierron F, Application of the virtual fields method to the identification of the homogeneous anisotropic hardening parameters for advanced high strength steels, International Journal of Plasticity, 2016, DOI: 10.1016/j.ijplas.2016.07.013.

Ghaffari Tari D, Worswick M J, Ali U, Gharghouri M A, Mechanical response of AZ31B magnesium alloy: experimental characterization and material modeling considering proportional loading at room temperature, International Journal of Plasticity, 2014, 55:247-267.

Ghaffari Tari D, Worswick M J, Elevated temperature constitutive behavior and simulation of warm forming of AZ31B, Journal of Material Processing Technology, 2015, 221:40-55.

Grytten F, Holmedal B, Hopperstad O S, Borvik T, Evaluation of identification methods for YLD2004-18p, International Journal of Plasticity, 2008, 24:2248-2277.

Guo X Q, Wu W, Wu P D, Qiao H, An K, Liaw P K, On the Swift effect and twinning in a rolled magnesium alloy under free-end torsion, Scripta Materialia, 2013, 69:319-322.

Harpell E T, Worswick M J, Finn M, Jain M, Martin P, Numerical prediction of the limiting draw ratio for aluminum alloy sheet, Journal of Materials Processing Technology, 2000, 100:131-141.

Hassannejadasl A, Rahmaan T, Green D E, Golvashchenko S F, Worswick M J, Prediction of DP600 flow surfaces at various strain-rates using Yld2004-18p yield function, Procedia Engineering, 2014, 81:1378-1383.

Hershey A V, the plasticity of an isotropic aggregate of anisotropic face centered cubic crystals, Journal of Applied Mechanics Transactions, 1954, ASME 21:241.

Hill R, A theory of the yielding and plastic flow of anisotropic metals. Proceeding of the Royal Society of London, Series A, 1948, 193:281-297.

Hill R, Theoretical plasticity of textured aggregates, Mathematical Proceedings of the Cambridge Philosophical Society, 1979, 85(1):179-191.

Hill R, A user-friendly theory of orthotropic plasticity in sheet metals. International Journal of Mechanical Sciences, 1993, 35:19-25.

Hosford W F, A generalized isotropic yield criterion, Journal of Applied Mechanics, 1972, 39:607-609.

45

Jenab A, Sari Sarraf I, Green D E, Rahmaan T, Worswick M J, The use of genetic algorithm and neural network to predict rare-dependent tensile flow behaviour of AA5182-O sheets, Materials and Design, 2016, 94:262-273.

Jonas J J, Ghosh C, Basabe V, Shrivastava S, The Hencky equivalent strain and its inapplicability to the interpretation of torsion testing experiments, Philosophical Magazine, 2012, 92(18):2313-2328.

Kaya S, Altan T, Groche P, Klopsch C, Determination of the flow stress of magnesium AZ31-O sheet at elevated temperatures using hydraulic bulge test, International Journal of Machine Tools & Manufacture, 2008, 48:550-557.

Kurukuri S, Worswick M J, Ghaffari Tari D, Mishra R K, Carter J T, Rate sensitivity and tension-compression asymmetry in AZ31B magnesium alloy sheet, Philosophical Transactions of the Royal Society of London A, 2014, 372:20130216.

Kuwabara T, Ikeda S, Kuroda K, Measurement and analysis of differential work hardening in cold-rolled steel sheet under biaxial tension, Journal of Materials Processing Technology, 1998, 80-81:517-523.

Lopes A B, Barlat F, Gracio J J, Ferreira Duarte J F, Rauch E F, Effect of texture and microstructure on strain hardening anisotropy for aluminum deformed in uniaxial tension and simple shear, International Journal of Plasticity, 2003, 19:1-22.

Onaka S, Equivalent strain in simple shear deformation described by using the Hencky strain, Philosophical Magazine Letters, 2010, 90(9): 633-639.

Peirs J, Verleysen P, Degrieck J, Novel technique for static and dynamic shear testing of Ti6Al4V sheet. Experimental Mechanics, 2012, 52:729-741.

Rahmaan T, Abedini A, Butcher C, Pathak N, Worswick M J, Experimental investigation of strain rate effect on fracture characteristics of DP600 and AA5182-O sheet metal alloys under shear loading, International Journal of Impact Engineering, 2017, DOI: 10.1016/j.ijimpeng.2017.04.006.

Rossi M, Pierron F, Stamborska M, Application of the virtual fields method to large strain anisotropic plasticity, International Journal of Solids and Structure, 2016, 97-98:322-335.

Safaei M, Zang S, Lee M, De Waele W, Evaluation of anisotropic constitutive models: mixed anisotropic hardening and non-associated flow rule approach, International Journal of Mechanical Sciences, 2013, 73:53-68.

Sivanandam S N, Deepa S N, An introduction to Genetic Algorithms, Springer, 2008.

Souto N, Thuillier S, Andrade-Campos A, Design of an indicator to characterize and classify mechanical tests for sheet metals, International Journal of Mechanical Sciences, 2015, 101-102: 252-271.

Souto N, Andrade-Campos A, Thuillier S, Mechanical design of a heterogeneous test for material parameters identification, International Journal of Material Forming, 2016a, DOI: 10.1007/s12289-016-1284-9.

Souto N, Andrade-Campos A, Thuillier, A numerical methodology to design heterogeneous mechanical tests, International Journal of Mechanical Sciences, 2016b, 107:264-276.

Steglich D, Tian X, Bohlen J, Kuwabara T, Mechanical testing of thin sheet magnesium alloys in biaxial tension and uniaxial compression, Experimental Mechanics, 2014, 54:1247-1258.

Steglich D, Tian X, Besson J, Mechanism-based modelling of plastic deformation in magnesium alloys, Europian Journal of Mechanics/ A Solids, 2016, 55:289-303.

Stoughton T B, A non-associated flow rule for sheet metal forming, International Journal of Plasticity, 2002, 18:687-714.

Swift H, Length changes in metals under torsional overstrain, Engineering, 1947, 163:253-257.

Tardif N, Kyriakides S, Determination of anisotropy and material hardening of aluminum sheet metal, International Journal of Solids and Structure, 2012, 49:3496-3506.

van den Boogaard A H, Thermally enhanced forming of aluminum sheet, modeling and experiments, PhD thesis, 2002, University of Twente, The Netherlands.

47

Yoon J W, Barlat F, Dick R E, Chung K, Kang T J, Plane stress yield function for aluminum alloy sheets, part II: FE formulation and its implementation, International Journal of Plasticity, 2004, 20:495-522.

Yoon J W, Barlat F, Dick R E, Karabin M E, Prediction of six or eight ears in a drawn cup based on a new anisotropic yield function, International Journal of Plasticity, 2006, 22:174-193.

Zang S L, Thuillier S, Le Port A, Manach P Y, Prediction of anisotropy and hardening for metallic sheets in tension, simple shear and biaxial tension, International Journal of Mechanical Sciences, 2011, 53:338-347.

Zhou X, Tamma K K, On the applicability and stress update formulations for corotational stress rate hypoelasticity constitutive models, 2003, Finite Elements in Analysis and Design 39:783-816.